COMPUTATIONAL ANALYSIS
OF THE
SSME FUEL PREBURNER FLOW

Final Report, Contract NAS8-35509
Report No. CI-FR-0084

Prepared For:

National Aeronautics and Space Administration
George C. Marshall Space Flight Center
Marshall Space Flight Center, AL 35812

By:

Ten-See Wang
Richard C. Farmer

CONTINUUM, Inc.
4715 University Drive
Suite 118
Huntsville, AL 35816-3405

February 25, 1986

TABLE OF CONTENTS

TABLE OF FIGURES

SUMMARY

The objective of this study was to develop a computational fluid dynamics model which simulated the steady state operation of the SSME fuel preburner. Specifically, the model will be used to quantify the flow factors which cause local hot spots in the fuel preburner in order to recommend experiments whereby the control of undesirable flow features can be demonstrated. This report presents the results of a two year effort to model the preburner. In this effort, investigating the fuel preburner flowfield, the appropriate transport equations were numerically solved for both an axisymmetric and a three-dimensional configuration. Continuum's **VAST** (VAriational Solution of the Transport equations) code, in conjunction with our CM-1000 Engineering Analysis Workstation and the NASA/Ames CYBER 205, was used to perform the required calculations.

This analysis concludes that the preburner operational anomalies are not due to steady state phenomena and must, therefore, be related to transient operational procedures.
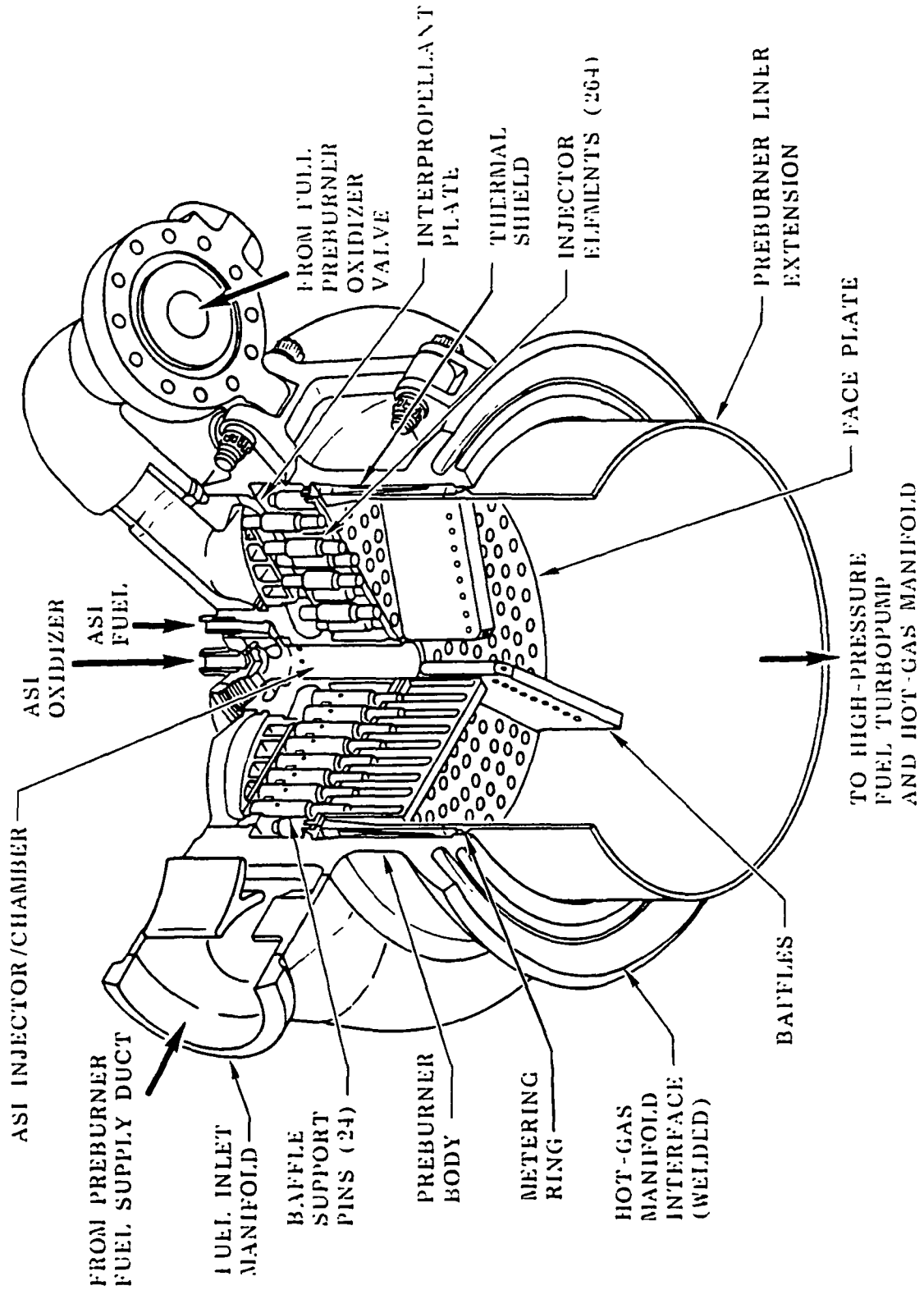
INTRODUCTION

The fuel preburner of the space shuttle main engine (SSME), as shown schematically in Fig. 1, consists of three major parts: the augumented spark igniter (ASI), injectors and the combustion chamber. The fuel preburner itself is structurally supported by the hot gas manifold to which it is welded and is a fuel cooled, double-walled chamber in which hot gas (hydrogen-rich steam) is generated to power the high pressure turbopump. The ASI initiates the combustion of the gaseous hydrogen fuel and liquid oxygen near the injector elements on the faceplate. The fuel preburner operates at a high pressure of 5547.5 PSI and a temperature of 2000 °R after the gas/liquid propellants are mixed and combusted. The preburned fuel then flows over a circular dome of the high-pressure fuel turbopump (HPFTP) and into a flow passage of about one-third of the original cross sectional area where it drives the turbines of the turbopump. These severe operating conditions include the effects of incomplete mixing of the propellants and of possible valve transient effects which can also produce local hot spots in the fuel preburner.

The concept of this modeling effort was to describe the bulk of the preburner flowfield. Local hot spots at the stagnation point on the turbopump dome and on turbine blades may be investigated with this model. The cause of the hot spots on the dome of the turbopump was suspected to be poor mixing of the oxygen injected in the ASI, i.e. a near-stoichiometric, hot streamline down the preburner centerline. Hot spots on turbine blades are more difficult to explain, especially since some evidence of free oxygen has also been observed. Modest radial and circumferential temperature variations are expected at the turbine blades, but oxygen should be consumed under the very fuel-rich flow conditions. Oxygen atomization and reaction should be rapid, and recent Rocketdyne studies have confirmed that this is indeed the case (Ref. 2). Those studies (Ref. 2) indicated that the oxygen was completely consumed in about one-third of a baffle length in the streamwise direction. Instantaneous oxygen rich flows during start up are believed by these authors to be the most likely source of turbine blade hot spots. Based on these observations, a preburner model was developed.

The fuel preburner flowfield was calculated from a surface just downstream of the injectors to the turbopump entrance. Groups of injectors were lumped to provide inflow to computational node points so that multiple grid points per injector would not be required. Upstream boundary conditions were developed such that flow into the boundary

FUEL PREBURNER

ASI INJECTOR/CHAMBER

FROM FULL PREBURNER OXIDIZER VALVE

INTERPROPELLANT PLATE

THERMAL SHIELD

INJECTOR ELEMENTS (264)

PREBURNER LINER EXTENSION

FACE PLATE

ASI OXIDIZER

ASI FUEL

TO HIGH-PRESSURE FUEL TURBOPUMP AND HOT-GAS MANIFOLD

FROM PREBURNER FUEL SUPPLY DUCT

FUEL INLET MANIFOLD

BAFFLE SUPPORT PINS (24)

PREBURNER BODY

METERING RING

HOT-GAS MANIFOLD INTERFACE (WELDED)

BAFFLES

Fig. 1   Schematic of SSME Fuel Preburner

From Reference (1)

nodes was represented with an orifice relation to relate hydrogen and oxygen manifold pressure to local flow rates during steady operation. Delays in propellant vaporization and combustion were investigated and found to be neglible. Mixing near the injectors was described by the injector/lumping analysis; downstream mixing was by turbulent transport only. The wall-cooled boundary layers were not modeled in this study. The upstream boundary conditions were designed so that they could be used directly with an unsteady analysis of the propellant manifolds. The numerical solution employed is also unsteady, so the description of the manifold feed is all that is required to provide a completely transient analysis. To investigate the fuel preburner flowfield, the appropriate transport equations were numerically solved for both an axisymmetric grid system and a three-dimensional system. Continuum's VAST (VAriational Solution of the Transport equations) computer code was used to model the flowfield.

VAST METHODOLOGY

Transport Equations

The VAST transport equations are written and solved in integral form (Ref. 3).

Conservation of Species

$$\frac{\partial}{\partial t} \int_V \rho_i \, dV = - \int_S (\rho_i \bar{q} + \bar{J}_i) \cdot d\bar{S} ; \qquad i = 1,\ldots,m \quad (1)$$

Where m is the number of species, ρ is the density, $\bar{q}$ is the velocity vector, $\bar{J}_i$ is the mass diffusive term, t is time and $d\bar{S}$ is the differential surface vector, while dV is the differential volume.

Conservation of Momentum

$$\frac{\partial}{\partial t} \int_V \rho\bar{q} \, dV = - \int_S (\rho\bar{q}\bar{q} - \bar{\bar{\sigma}}) \cdot d\bar{S} \qquad (2)$$

Where $\bar{\bar{\sigma}}$ is the stress tensor.

Conservation of Energy

$$\frac{\partial}{\partial t} \int_V \rho E \, dV = - \int_S (\rho E \bar{q} - \bar{\bar{\sigma}} \cdot \bar{q} + \bar{Q} + \bar{\beta}) \cdot d\bar{S} \qquad (3)$$

Where E is the intensive total energy, $\bar{Q}$ is the conductive heat flux vector and $\bar{\beta}$ is the heat transferred by mass diffusion.

The Numerical Analog

The VAST transport equations may be generalized as:

$$\frac{\partial}{\partial t} \int_V U_j \, dV = - F_j \; ; \qquad\qquad j = 1, \ldots, J \quad (4)$$

Where J is the total number of transport equations and

$$U = \begin{bmatrix} \rho_i \\ \rho\bar{q} \\ \rho E \end{bmatrix} \; ; \quad F = \int_S \begin{bmatrix} (\rho_i \bar{q} + \bar{J}_i) \cdot d\bar{S} \\ (\rho\bar{q}\bar{q} - \bar{\bar{\sigma}}) \cdot d\bar{S} \\ (\rho E\bar{q} - \bar{\bar{\sigma}} \cdot \bar{q} + \bar{Q} + \bar{\beta}) \cdot d\bar{S} \end{bmatrix} \qquad (5)$$

The integration domain may be subdivided into E finite elements and the VAST equations reduced to :

$$\sum_{e=1}^{E} (\Delta U_j \Delta V / \Delta t)_e = - \sum_{e=1}^{E} F_{j,e} \qquad\qquad (6)$$

The flux $F_{j,e}$ is evaluated over the surface of the elements and $(\Delta U_j \Delta V / \Delta t)_e$ is the total accumulation of the jth conserved quantity within element e. Since the sides of the element terminate in nodes at which the discretized conserved quantity are known at a previous time step, the new values of the conserved quantity at the next time step on the nodes depend upon the allocation from the accumulations within the elements. The conserved quantity at a node is therefore determined by assembling the contributions from its surrounding elements. That is

$$(\Delta U_j \Delta V / \Delta t)_n = - \sum_{e=1}^{k} \xi_{j,e,n} F_{j,e} \qquad\qquad (7)$$

Where n is the node number, k is the total number of elements surrounding the node and $\xi_{j,e,n}$ is an allocation parameter.

The assembled equation (7) is analogous to a finite difference expression in which the spatial transformations are numerically imbedded in the analog. It may be interpreted as a general form of the finite difference scheme since different finite difference schemes can be derived with selected allocation parameters. Allocation parameters determine the differencing scheme and the stability of the system.

VAST Differencing Scheme

The VAST differencing scheme is different from any existing schemes in that it does not dictate a fixed allocation parameter throughout the course of integration, but changes this parameter dynamically according to the variational principal of the real fluid system. The original algorithm (Ref. 3) was based upon the satisfaction of the Second Law of Thermodynamics. The advanced development (Ref. 4) requires that the rate of entropy producton be maximized. It is a stronger argument than the Second Law, since if the production rate of entropy is a maximum, it has to be greater than (or equal to) that required by the Second Law. The VAST differencing scheme thus uses the transport equations as equality constraints, subject to the objective of maximizing the entropy production rate while dynamically determining the allocation parameters such that maximum stability of the system can be achieved.

TURBULENCE MODELING

Turbulence modeling involves the mathematical closure of the Reynolds stress terms which result from time averaging the Navier-Stokes equations. Numerous turbulence models have been developed in the recent years (Ref. 5). These models vary in complexity and in their ability to accurately represent various flowfields. The turbulence parameters in the models were determined empirically for the closure of one or more systems, but are not necessarily applicable to other systems. Furthermore, complicated turbulence modeling may introduce instability in numerical solutions. Since the preburner flowfield is far more complicated than any other system for which turbulence parameters have been determined, a straightforward and simple eddy viscosity model with overall accuracy established by comparison to a single hydrogen/air coaxial jet (Ref. 6) was used in the preburner calculations.

The effects of turbulence are modeled by an eddy viscosity coefficient μ_T which enters into the laminar Navier-Stokes equation by replacing molecular viscosity μ_L by μ where

$$\mu = \mu_L + \mu_T \tag{8}$$

The relationship between μ_T and μ_L is obtained from ducted turbulent flow

$$\ln(\mu_T/\mu_L) = 0.89936 \ \ln(Re) - 5.17515 \tag{9}$$

where Re is the Reynolds number, based on the diameter of the inner jet.

The eddy thermal conductivity K and eddy mass diffusivity D are determined through the input of the turbulent Prandtl number (Pr) and turbulent Schmidt Number (Sc).i.e.

$$Pr = \frac{C_p \mu}{K} \tag{10}$$

-7-

and

$$Sc = \frac{\mu}{D\rho} \tag{11}$$

For a single coaxial jet, the potential core length of the inner jet, Xc, is determined through Abramovich's empirical formula (Ref. 7). X approaches Xc when r_{1p} approaches zero.

$$\frac{r_{1p}}{r_1} = 1 - L\frac{X}{r_1} \tag{12}$$

and

$$L = \pm \frac{0.27(1-m)(0.214+0.144m)^{\frac{1}{2}}}{(1+m)} \tag{13}$$

where m is the ratio of the outer flowspeed to the inner flowspeed. In calculating L, a minus sign is taken when m is greater than unity; r_1 is the radius of the inner tube and r_{1p} is the radius of the central potential core.

Turbulent eddy viscosities can be determined through equation (9) for the inner flow Reynolds number Re_{inner} and the outer annular flow Reynolds number Re_{outer}. The Re_{outer} is based on hydraulic radius. The eddy viscosity model is then given by

$$\mu_T = \begin{cases} \mu_T(Re_{inner}) & \text{at } X \leq X_c \\ \dfrac{\mu_T(Re_{outer}) - \mu_T(Re_{inner})}{\ln \dfrac{\mu_T(Re_{outer})}{\mu_T(Re_{inner})}} & \text{at } X > X_c \end{cases} \tag{14}$$

RESULTS OF THE SINGLE COAXIAL HYDROGEN/AIR JET CALCULATION

Axisymmetric calculations were conducted for the turbulent mixing of a parallel coaxial hydrogen/air jet (Ref. 6). The inner hydrogen jet Mach number was 0.9 and the outer air jet Mach number was 1.32. An initial velocity profile was given for the inlet condition. A potential core length of 7.7 inner jet nozzle diameters was obtained through equation 12 and 13. Previous calculations (Ref. 8) used a grid system of 45 by 29 nodes and reservoir upstream boundary conditions (RUBC). The results showed some oscillations in the potential region for both the centerline velocity decay profile and the lateral velocity profiles. These oscillations were postulated to be caused by the combination of the coarse grid (9 longitudinal nodes in the potential region) and the RUBC.

A grid system of 53 by 30 nodes (15 longitudinal nodes in the potential region) with fixed table value upstream boundary conditions (FTVUBC) was rerun for this report. Figure 2 shows the comparison of this new centerline velocity decay prediction against the axial distance. Excellent matches of the predictions with the experimental data were obtained. Previous centerline velocity decay is shown in Fig. 3 for comparison. Figure 4 shows the results of radial velocity and radial hydrogen mass fraction profiles at seven different stations. The comparisons of the computational results with the experimental data were quite good for a two "global" turbulence-level model. The good agreement in radial profiles is not surprising since Chriss and Paulk (Ref. 9) have also obtained good results with a constant radial eddy viscosity for these jets.

The improvement of this calculation over the previous one is believed to be due more to the upstream boundary condition than the grid density. The inherent mass flow rate fluctuation at the inlet caused by RUBC (Ref. 8) created oscillations in the flowfield and also made it difficult for the calculation to converge.
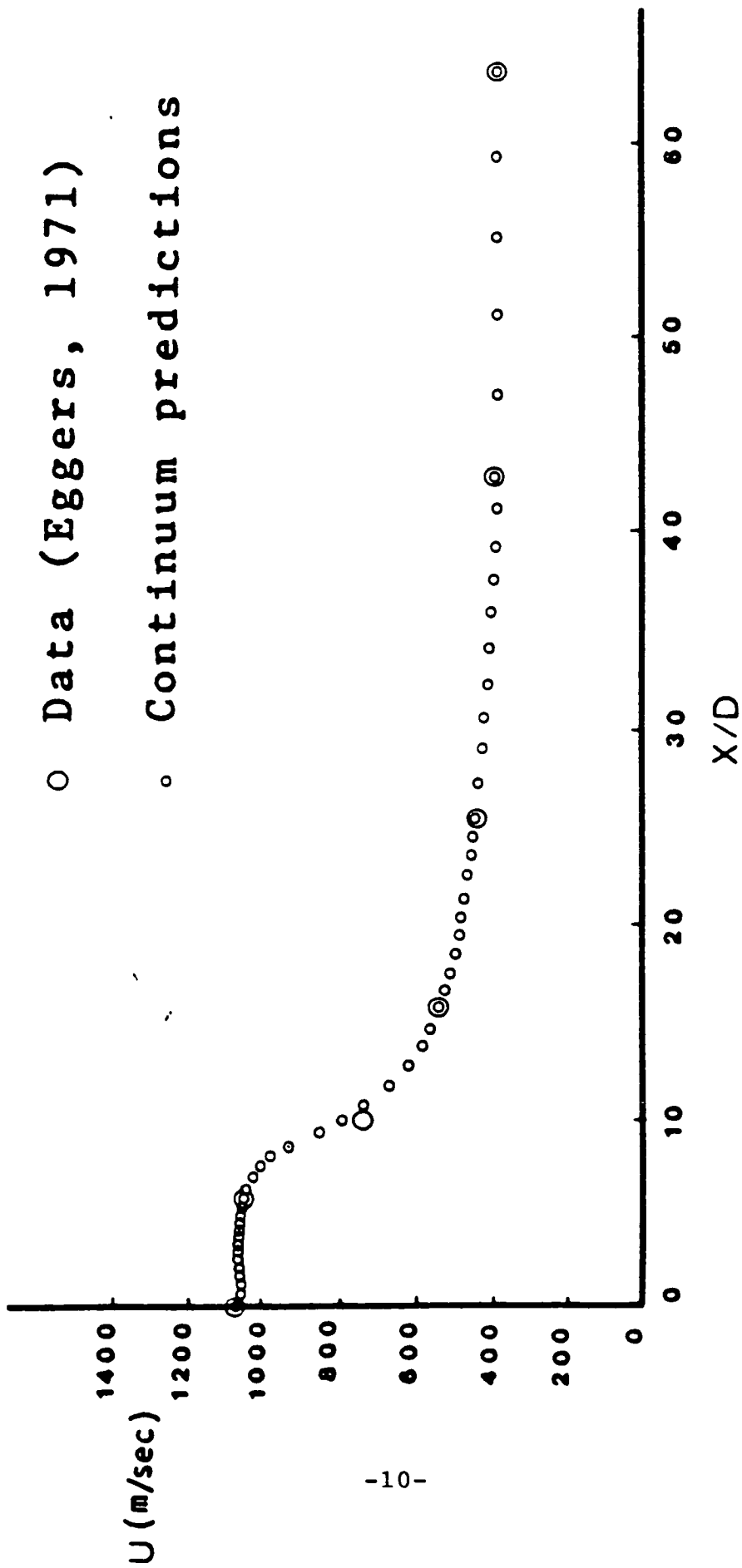
Fig. 2   Centerline Velocity Decay of a Coaxial H_2/Air Jet
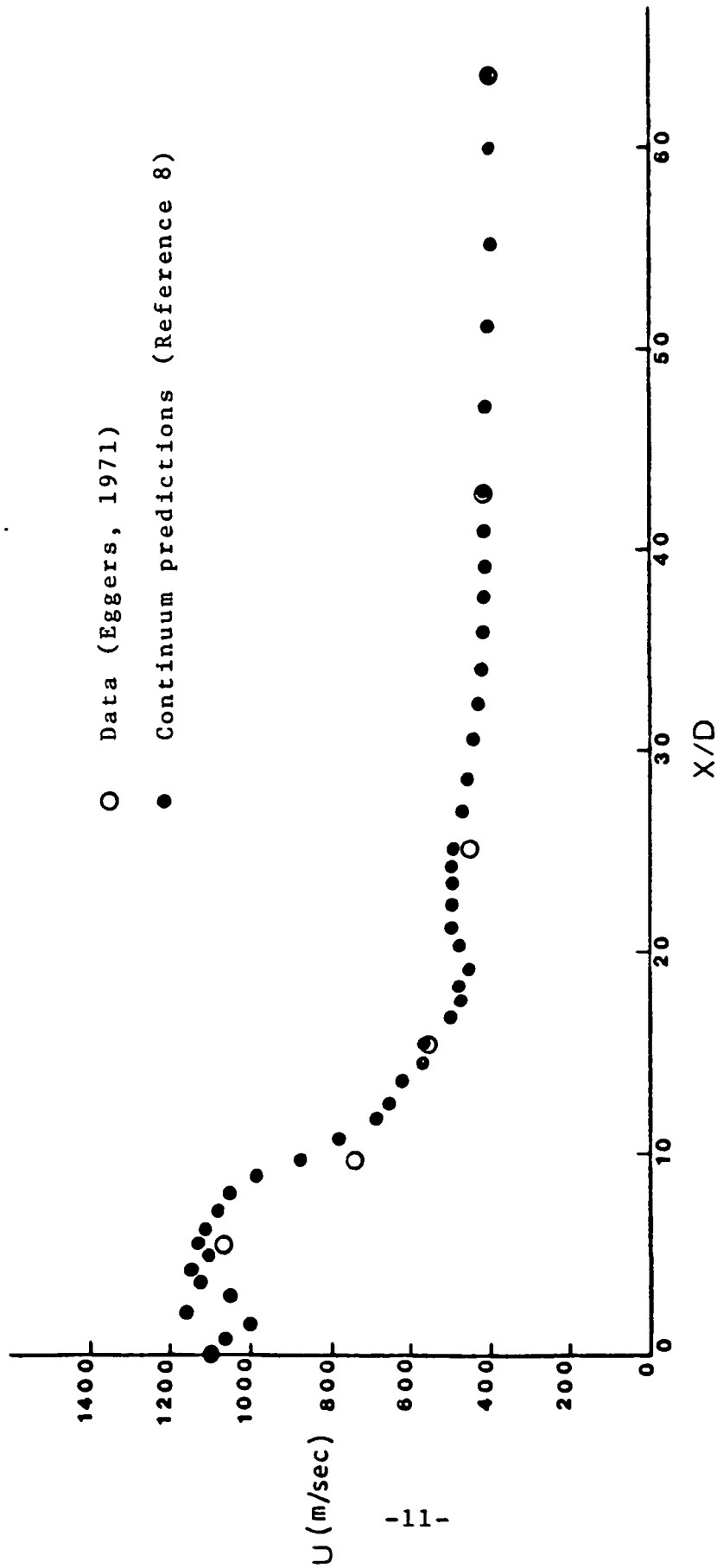
Fig. 3   Centerline Velocity Decay of a Coaxial H_2/Air Jet   From Reference 8
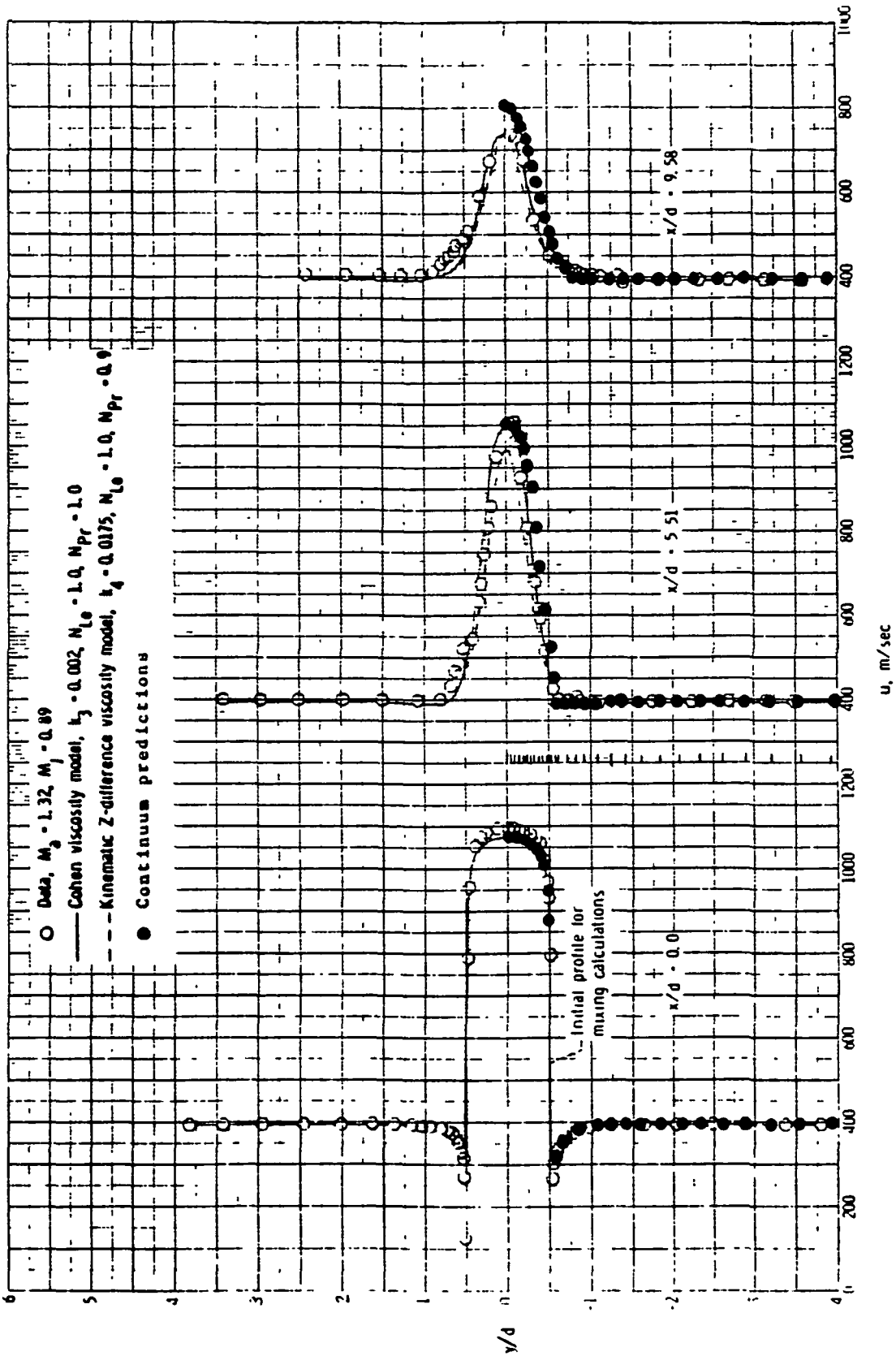
Fig. 4   (a) Velocity profiles; x/d = 0.0 to 9.58.
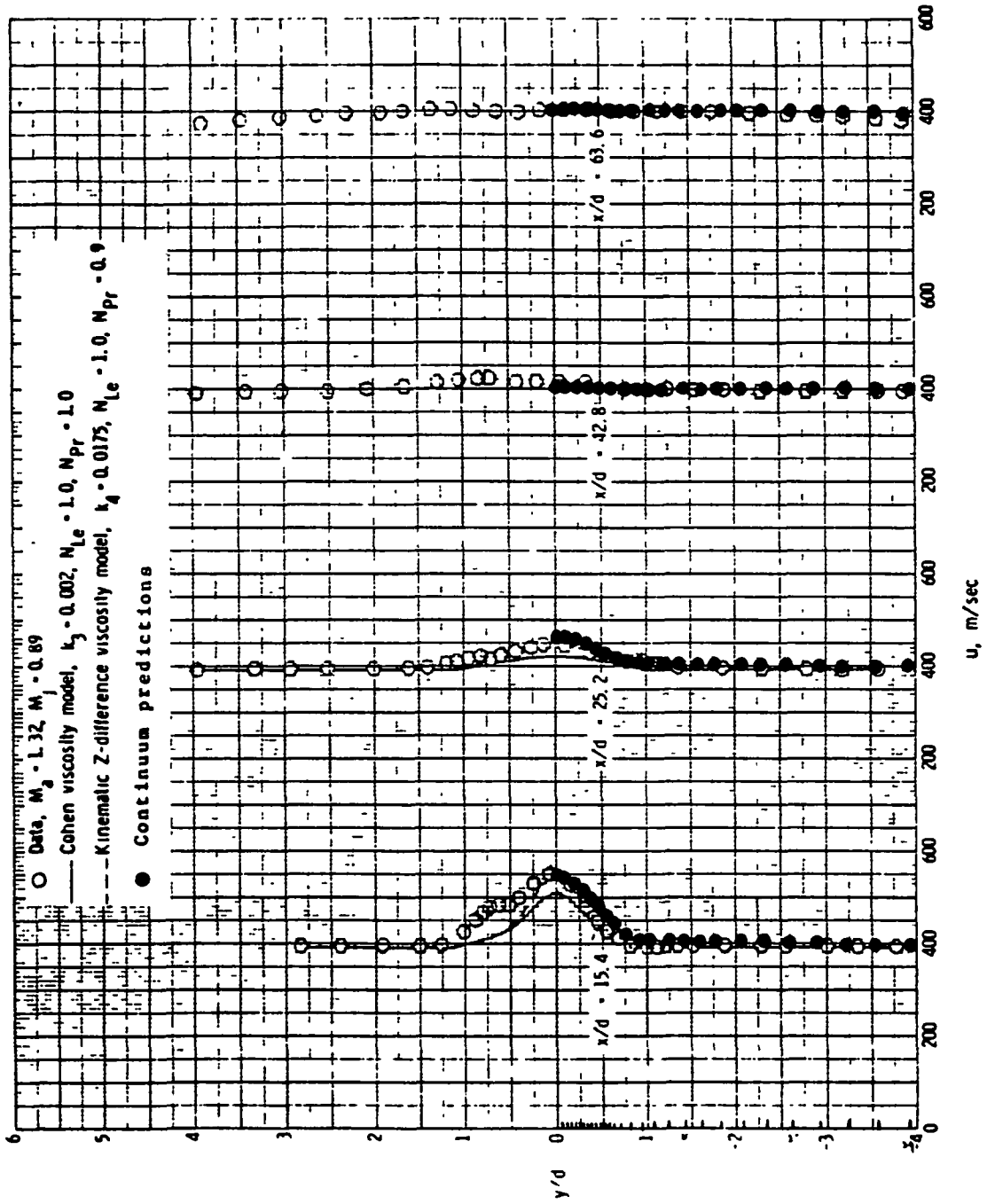
Hydrogen-air mixing data and correlation for M_a = 1.32.
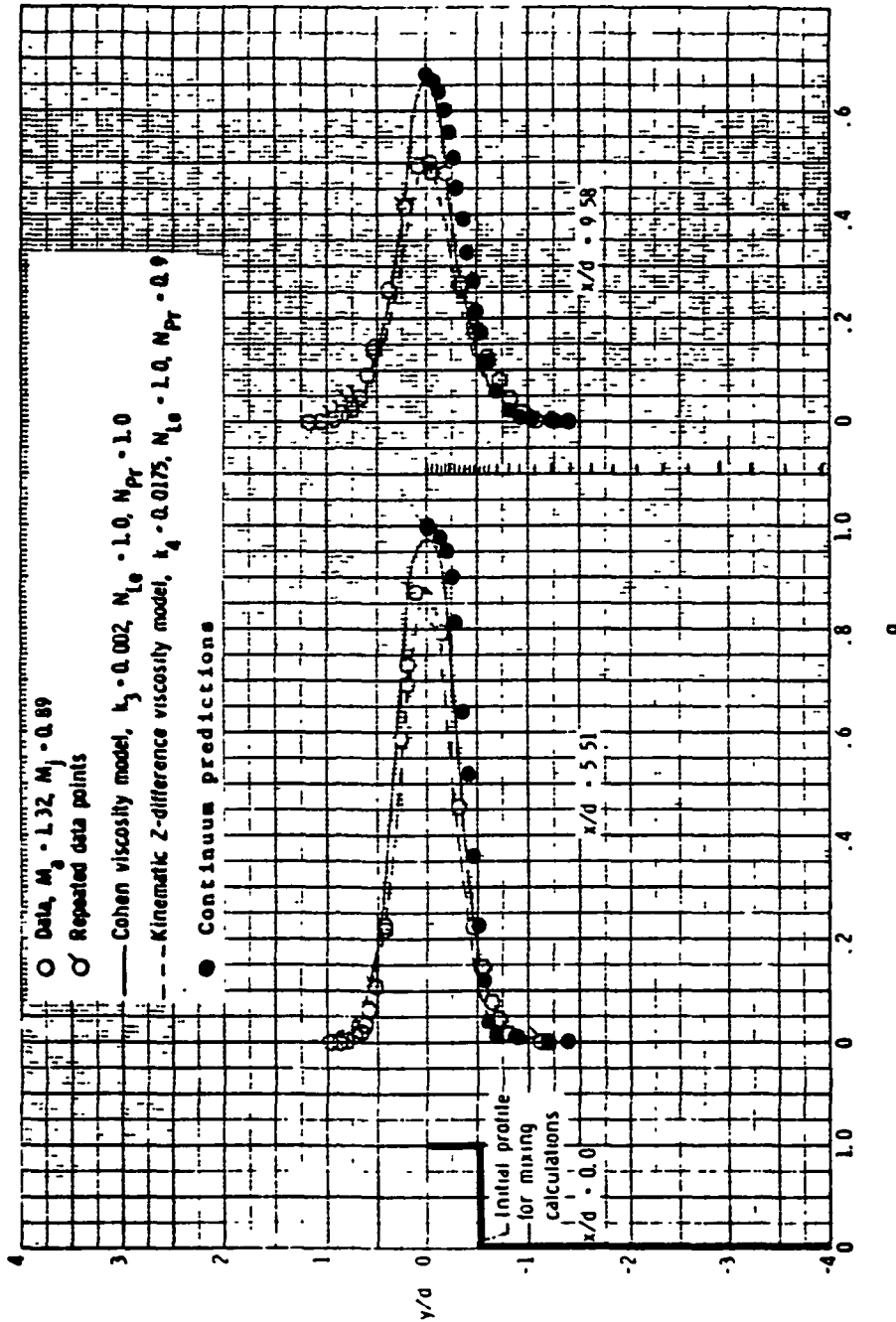
Fig. 4   (b) Velocity profiles; x/d = 15.4 to 63.6.

-13-

Fig. 4 (c) Hydrogen mass fraction profiles; x/d = 0.0 to 9.58.

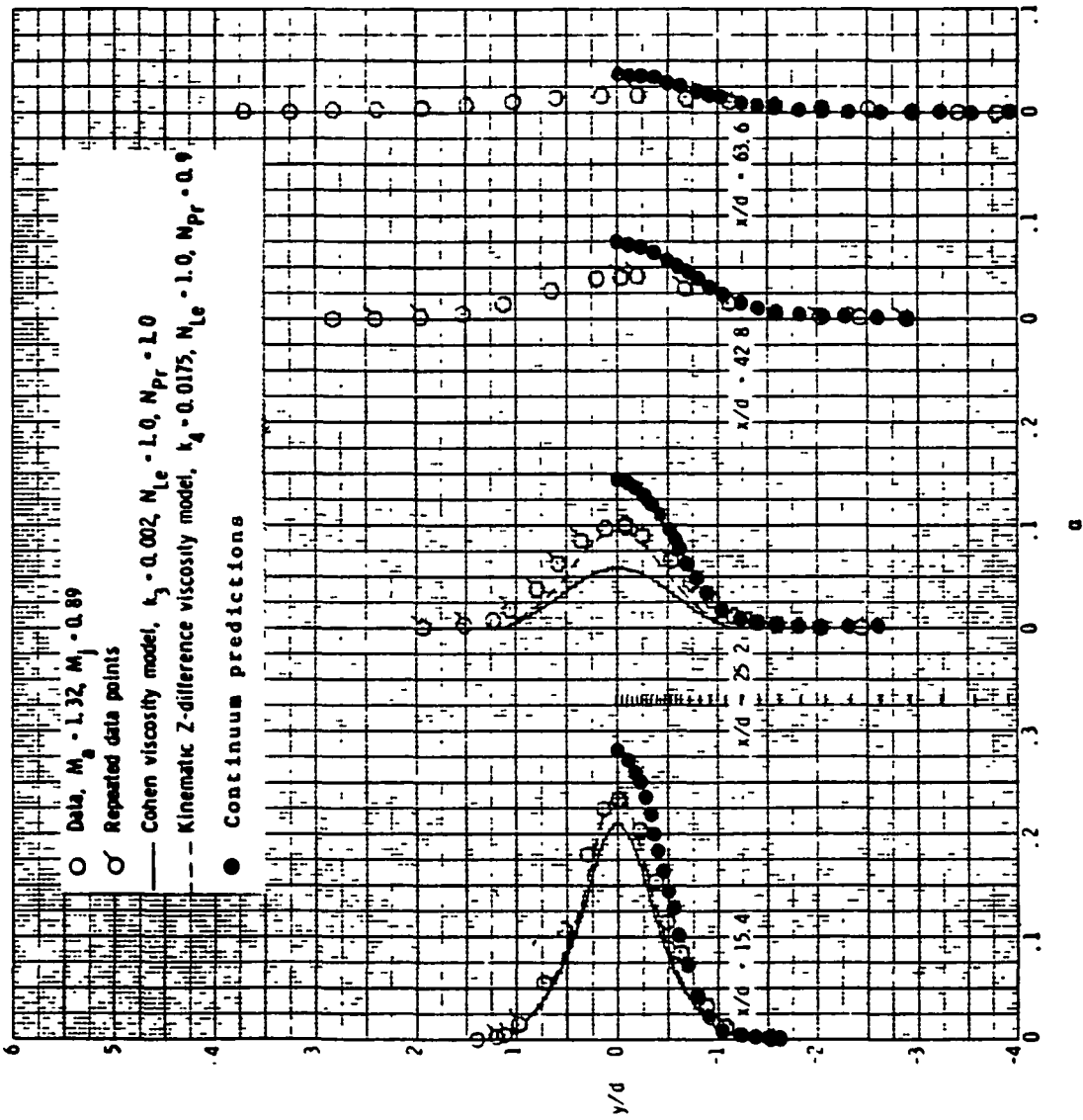Fig. 4   (d) Hydrogen mass fraction profiles;   x/d = 15.4 to 63.6.

COMBUSTION CHEMISTRY

Atmospheric pressure hydrogen/oxygen combustion kinetics were reviewed (Refs. 10, 11), and the chemical kinetics rates suggested that the hydrogen/oxygen are expected to combust very fast at higher pressures.

A one-step, reversible finite rate chemical kinetics model with Arrhenius rate expression is developed in this study.

$$\text{REACTION} \qquad H_2 + \frac{1}{2} O_2 = H_2 O \qquad\qquad (15)$$
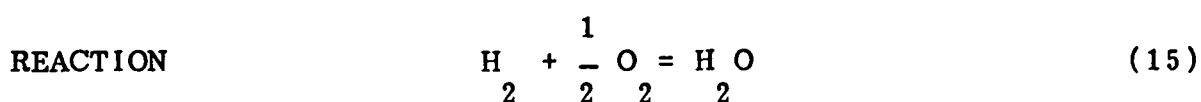
The reaction rate of this model is verified in Fig. 5 and Fig. 6 for hydrogen/air ignition delay time comparisons with a detailed twenty-eight reaction mechanism (Ref. 11). The temperature histories of these two models agreed well at equivalence ratios of one and two. These two figures also revealed that hydrogen/oxygen reaction is very fast and the ignition delay times of hydrogen/air at rich combustion (ϕ =2) is very close to those at stoichmetric combustion.

This one-step, reversible finite rate chemical kinetics model was then used to predict the ignition delay times for hydrogen/oxygen combustion at the fuel preburner operating conditions (ϕ =7.4). The ignition delay time at fuel preburner operating pressure (377 atm), as shown in Fig. 7, is much shorter than that at atmospheric pressure; it is practically instantaneous.

TEMPERATURE HISTORIES FOR H₂/AIR AT 1 ATM (∅ = 1)

- - - - - ROGERS & CHINITZ 28 RXN MECHANISM
————— CONTINUUM 1 STEP RXN MECHANISM
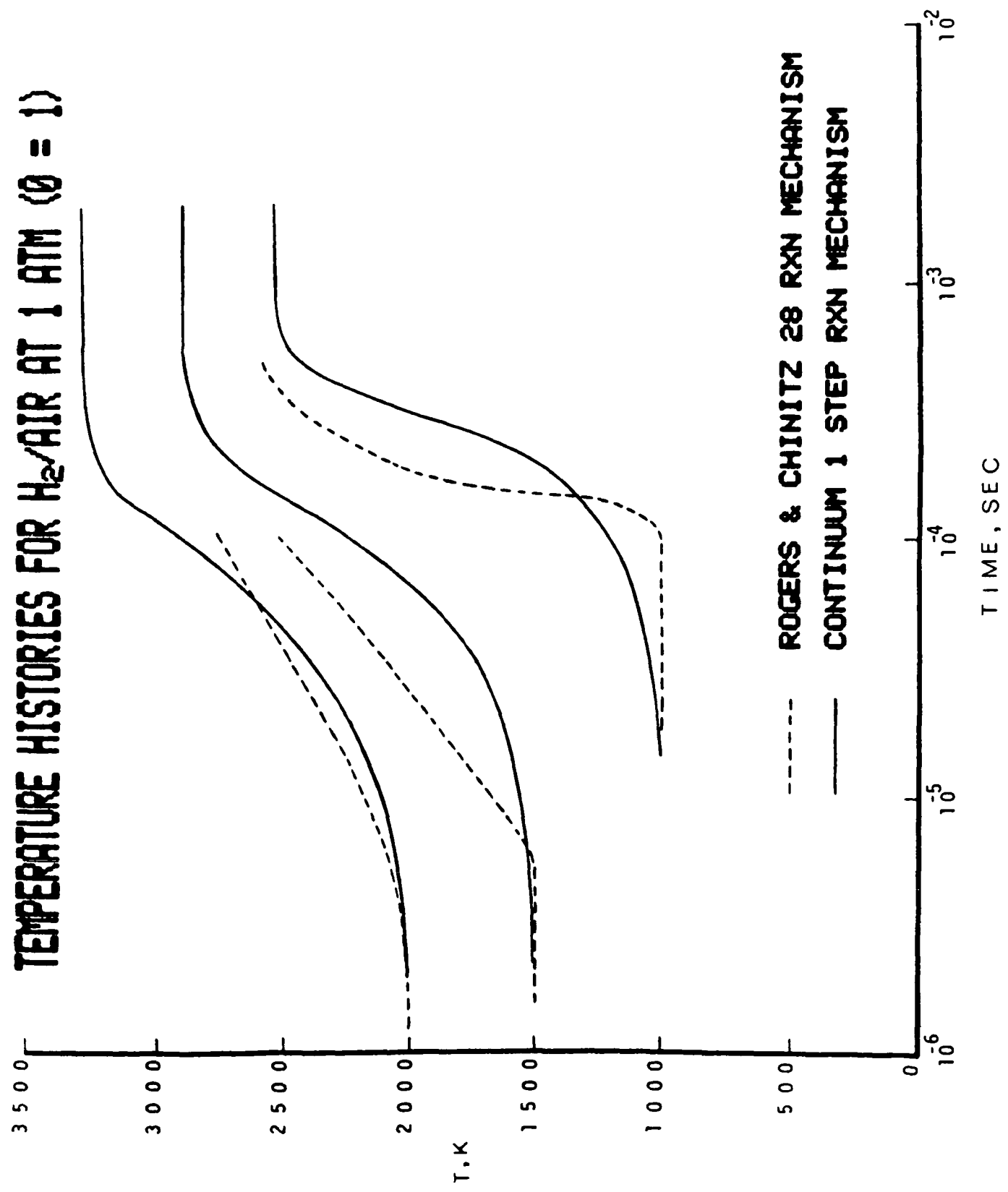
Fig. 5 Temperature Histories for H_2/Air at 1 ATM ($\emptyset$ = 1)

TEMPERATURE HISTORIES FOR H_2/AIR AT 1 ATM ($\emptyset$ = 2)

T,K

TIME,SEC

----- ROGERS & CHINITZ 28 RXN MECHANISM
——— CONTINUUM 1 STEP RXN MECHANISM
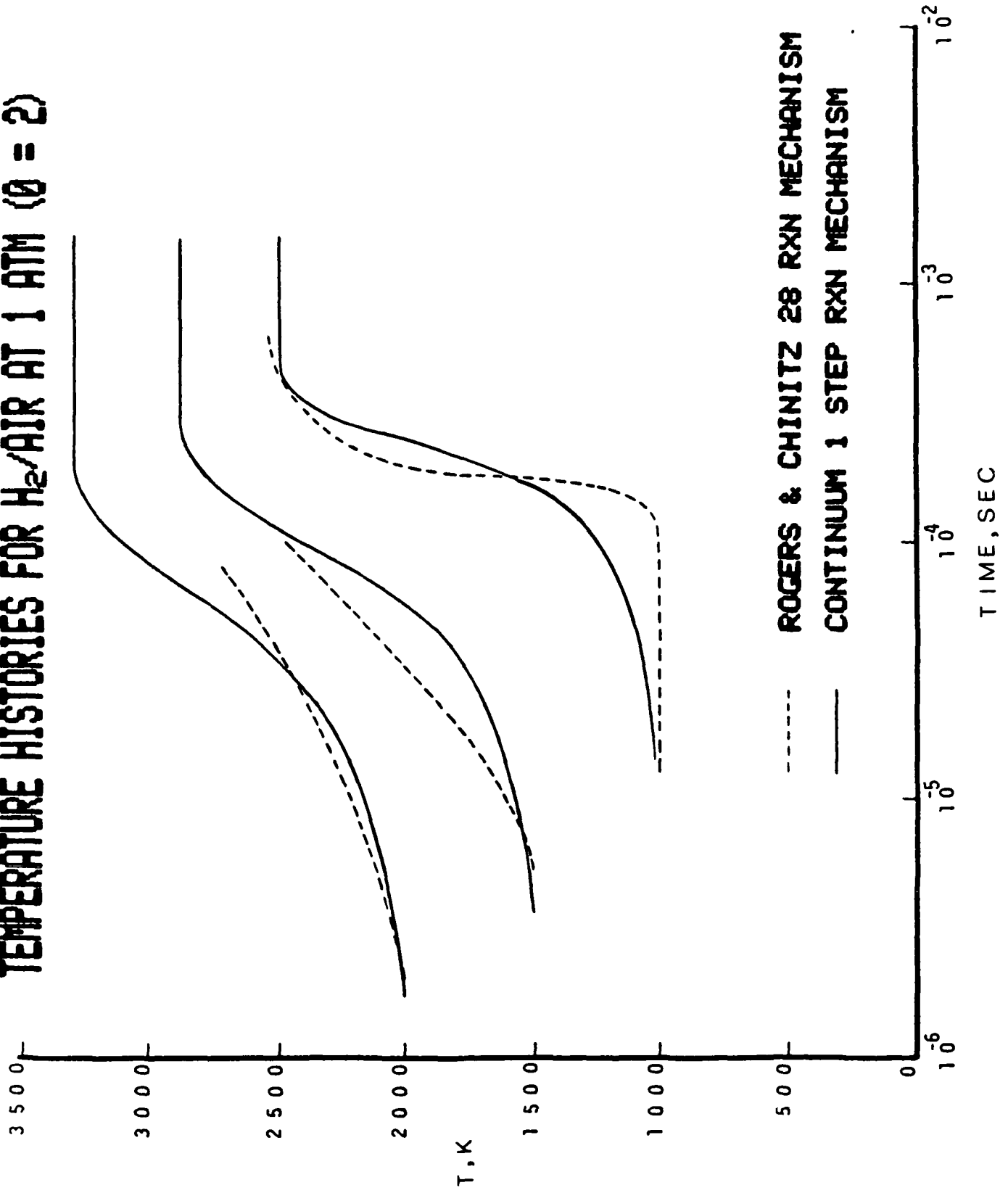
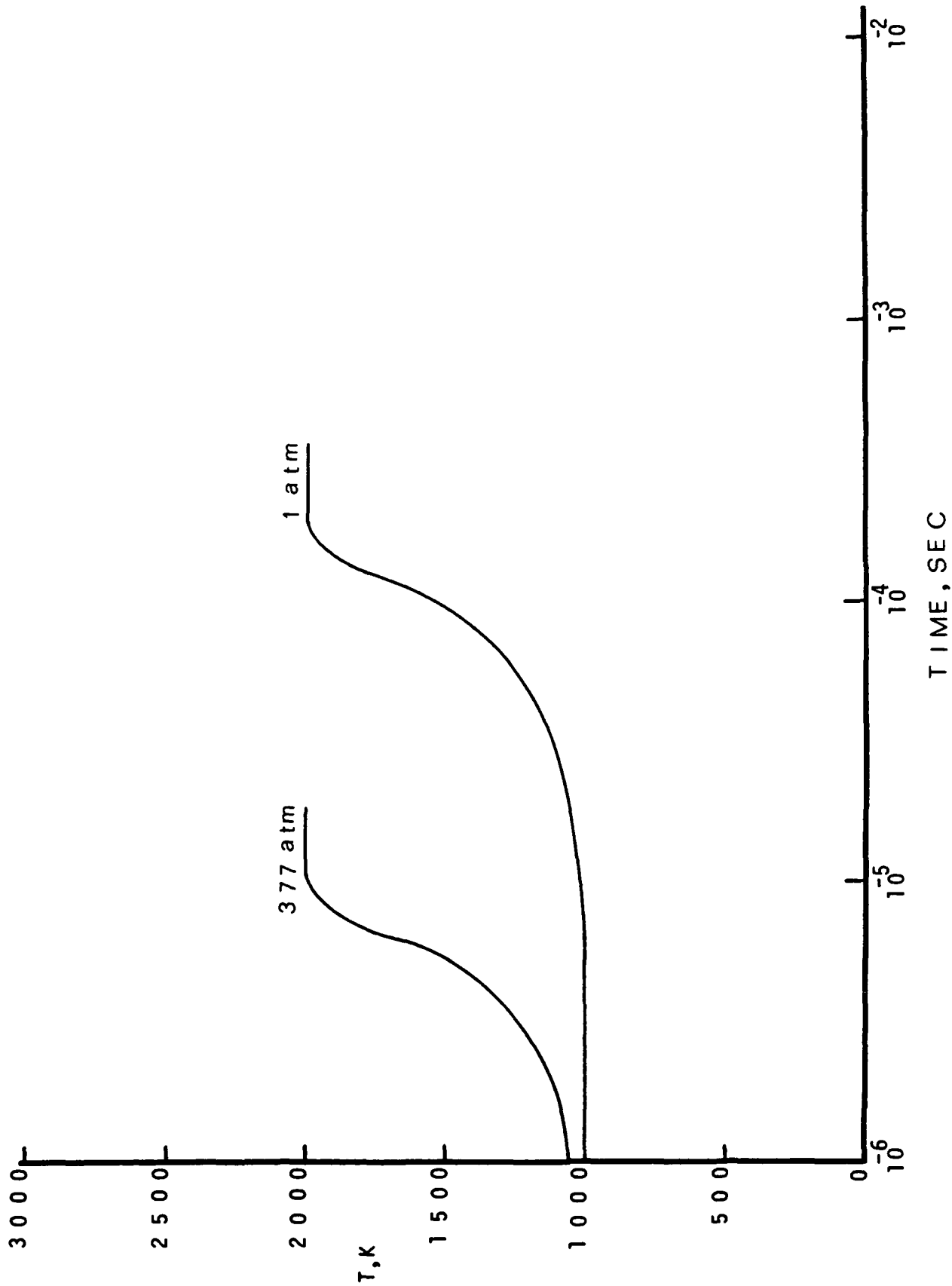Fig. 6 Temperature Histories for H_2/Air at 1 ATM ($\emptyset$ = 2)

Fig. 7 Temperature Histories for H_2/O_2 at $\phi = 7.4$

SUBSONIC BOUNDARY CONDITIONS

The fluid flow in the SSME fuel preburner is not only subsonic, but also has large temperature gradients between the neighboring jets across the injector faceplate. Previous studies (Ref. 8) have found that a fixed table value upstream boundary condition (FTVUBC) in conjunction with a fixed integrated mass flow rate downstream boundary condition is appropriate to describe the complicated subsonic preburner flowfield. The fixed integrated mass flow rate downstream boundary condition regulates the steady state mass flow rate throughout the fuel preburner flowfield, and the FTVUBC allows any pressure disturbance originating from downstream to pass through the inlet boundary. There is a loss of absolute conservation at the inlet and outlet boundary during the early stage of integration which rapidly damps the transient phenomena and pressure disturbances, but the flowfield resumes its absolute conservation as the computation reaches steady state.

In this report, an injector simulation upstream boundary condition (ISUBC) is developed to replace FTVUBC in order to better simulate the fuel preburner characteristics and to anticipate the potential importance of manifold flow upstream of the injector faceplate. The ISUBC has all the advantages of FTVUBC, yet further relates the mainfold pressure to the preburner pressure, thus it is a tailor made upstream boundary condition for the SSME fuel preburner simulation. The fixed integrated mass flow rate downstream boundary condition was used in conjunction with ISUBC during this computation. The methodology of the subsonic boundary conditions used in the fuel preburner calculation is described as follows.

Fixed Integrated Mass Flow Rate Boundary Conditions

1. Let ρ_i, ρq, ρE be free,

2. $\rho q^{n+1} = \rho q^n \dfrac{m_I}{\displaystyle\int_{exit} \rho q \, dA}$, superscript n+1 stands for the new time step,

3. $\rho u^{n+1} = \rho q^{n+1} \cos \theta$,

$\rho v^{n+1} = \rho q^{n+1} \sin \theta$,

where m_I is the inlet mass flowrate and θ means local flow angle.

This downstream boundary condition maintains a constant integrated mass flow rate at the exit. A mass balance ratio is determined between the inlet mass flow rate and the instantaneous exit integrated mass flow rate. This ratio is then applied to the mass flux on the exit plane to keep a constant integrated mass flow rate throughout the flowfield.

Injector Simulation Upstream Boundary Condition

The SSME fuel preburner injector elements and manifold may be lumped together and viewed as an orifice passage. The mathematical relationship between mass flow rate and pressure drop between the two ends of the orifice can be derived by a mechanical energy balance.

$$m = C_I \left[2\rho_o (P_o - P) \right]^{0.5} \tag{16}$$

Where C_I is an effective discharge coefficient and subscript $_o$ denotes manifold conditions. C_I can be estimated through steady state operating conditions or can be obtained experimentally. The formal procedure is described as follows:

1. Let ρ_i, ρq, ρE be free

2. $P = (\gamma - 1) (\rho E - \dfrac{1}{2} \dfrac{\rho q^2}{\rho})$

3. $\rho q^{n+1} = C_I [2\rho_o (P_o - P)]^{0.5} / S_c$

4. $\rho_i^{n+1} = \rho_{i,T}$

$\rho E^{n+1} = \rho E_T$

where γ is the ratio of specific heats and the subscript represents table values and S_c is the flow area.

5. Constant Flow Angle

Procedure 3 reveals that the ISUBC controls the flow rate at the injector face via the pressure drop between manifold and injector faceplate. The flow rate increases as the pressure at the injector face decreases and vice versa. The irreversibility of ISUBC makes it absorb pressure disturbances sent from downstream faster than the RUBC. The ISUBC regulates the mass flow rate instead of resetting it, therefore causing less disturbances than FTVUBC.

The ISUBC also has the potential for separate fuel and oxidizer inlet flow rate control, i.e., the injector manifold can be lumped into two or more orifices instead of one. Separate discharge coefficients can be determined for each orifice. ISUBC can also be applied to transient fuel preburner problems provided that the pressure histories in the manifold are given.

GENERAL FLOW FEATURES AND ASSUMPTIONS

The SSME fuel preburner consists of one ASI, 264 hydrogen/oxygen coaxial injector elements and 588 tiny hydrogen bleed holes on the injector faceplate which feed propellants into the combustion chamber. The major processes involved in this complicated operation are atomization, vaporization, combustion and mixing. The fuel preburner injector element is a baffled coaxial element that mixes the gaseous hydrogen and liquid oxygen in correct proportions and uniformly distributes and injects the propellants into the combustion chamber. The high velocity of the low density fuel, relative to the density and velocity of the oxidizer, would produce a high rate of atomization and thorough mixing (Ref. 1). It is then expected that the primary atomization of liquid oxidizer through the injector elements would be completed in a very short distance from the injector face. The operating variables of fuel preburner in Table 1 and the initial properties in Table 2 indicate that the propellants are "supercritical fluid" under these conditions. The atomized "supercritical fluid" drops would gasify themselves without undergoing phase change (Ref. 12), i.e., instantaneous vaporization or so called "shear stripping" (Ref. 13). The gasified and mixed propellants would react almost instantaneously under fuel preburner operation conditions, which will further help the atomization and mixing process due to the acceleration of the combusted gases.

Due to the very rapid nature of the initial mixing, vaporization and combustion processes, the atomization seems to be the rate controlling step which, in turn, could be assumed very fast due to the high rate of atomization at the injector element. The best engineering model to computationally represent the entire flowfield would be to model the injector faceplate with concentric annual rings. Each ring represents a combustion zone with fuel/oxidizer equivalence ratios determined by the layout of the injector faceplate. The properties of the concentric ring jets will be calculated from equilibrium calculations. The mixing of the ring jets will be simulated instead of resolving the interaction of each individual jet of the injector element or holes. Such a model is required because the resolution of the 264 injector elements and 588 hydrogen holes is beyond present computational capability for practical applications.

Figure 8 shows the layout of the injector elements and holes on the injector faceplate. Four major combustion zones can be grouped together according to the sizes and
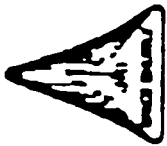
locations of the injector elements and holes. They are igniter zone, AB zone, CD zone and EFGH zone. The mass flow rate is assumed to be evenly distributed among all the injector elements and holes. There is an additional baffle flow zone the in three-dimensional model.

Table 1: Operating variables for fuel preburner at FPL of 1.09

	Pressure (PSIA)	Temperature ($^{\circ}$R)
Manifold Hydrogen Inlet	6023	278
Mainfold Oxygen Inlet	7135	213
Igniter Hydrogen Inlet	6781	102
Igniter Oxygen Inlet	7212	213
FPB Chamber	5547	1990

Table 2: Critical properties for hydrogen, oxygen and water

	Pressure (PSIA)	Temperature ($^{\circ}$R)
Hydrogen	188	60
Oxygen	732	278
Water	3199	1165

FUEL PREBURNER INJECTOR MODIFICATION

MOD – ☐

.033" DIA. (108)

.0396" DIA. (243)

.0466" DIA. (48)

.020" DIA. (18)

.046" DIA. (102)

.050" (66)

.125" DIA. (3)

INNER
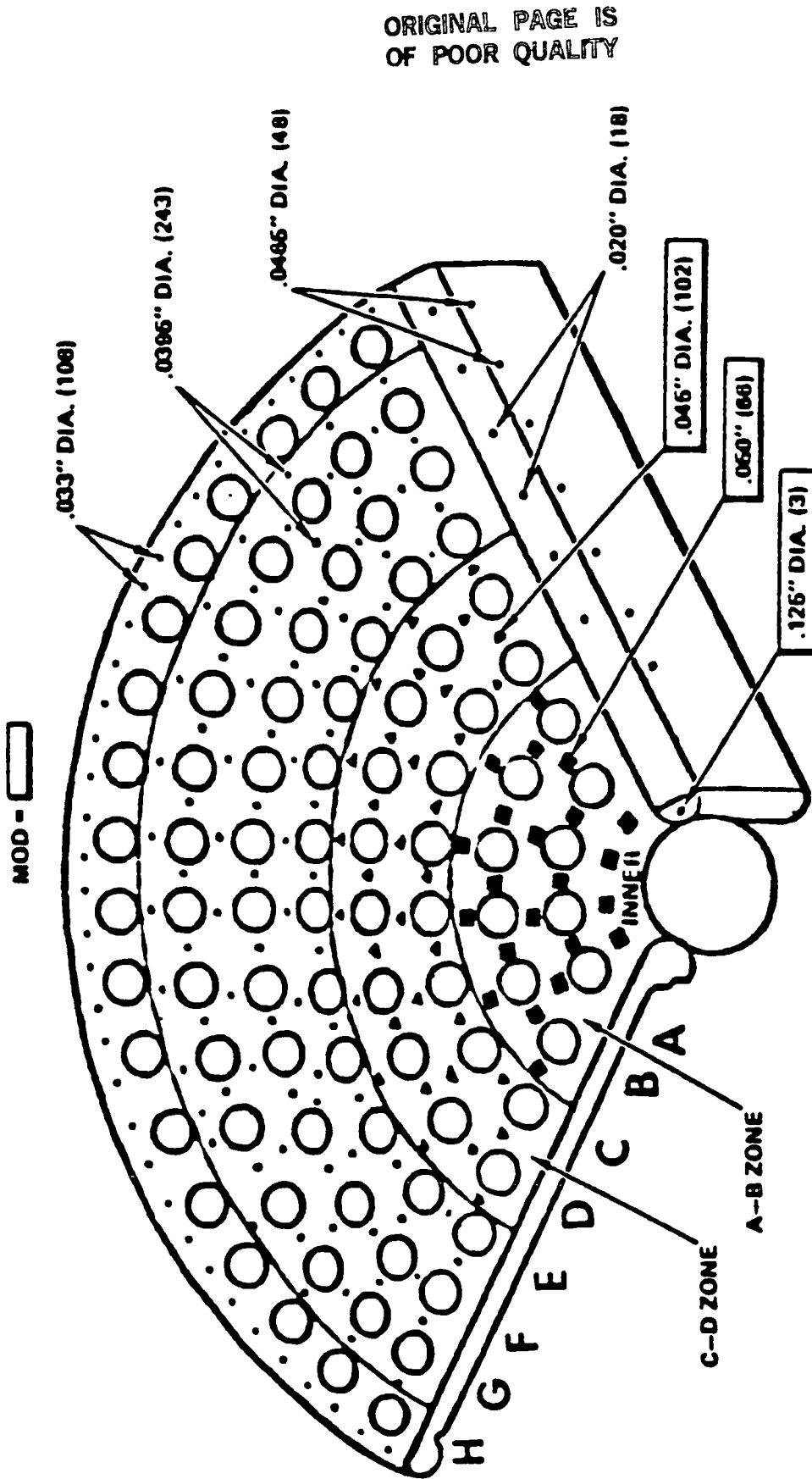
H G F E D C B A

C–D ZONE

A–B ZONE

Fig. 8   The Layout of SSME Fuel Preburner Injector Faceplate

-26-

AXISYMMETRIC MODELING OF THE FUEL PREBURNER

Grid Definition

Two grid systems were used in the axisymmetric fuel preburner calculations. The coarse grid definition, as shown in Fig. 9 was composed of two regions. Region I contains the igniter flow region and main combustion chamber between the injector face and 5.55 in. below the injector face. Region II covers the rest of the chamber. There are 540 nodes in Region I; 126 of them are null nodes. Region II has 350 nodes. The coarse grid definition therefore has 890 nodes in total; 764 of them are active nodes. The final grid definition, as shown in Fig. 10, is composed of three regions. Region I is the igniter flow region. Region II contains the combustion chamber between injector face and 5.55 in. below the injector faceplate. Region III covers the rest of the combustion chamber. There are 5,965 nodes in the fine grid definition. Region I has 160 nodes, region II has 1,800 nodes and Region II has 4,005 nodes. No null nodes were used for the fine grid definition.
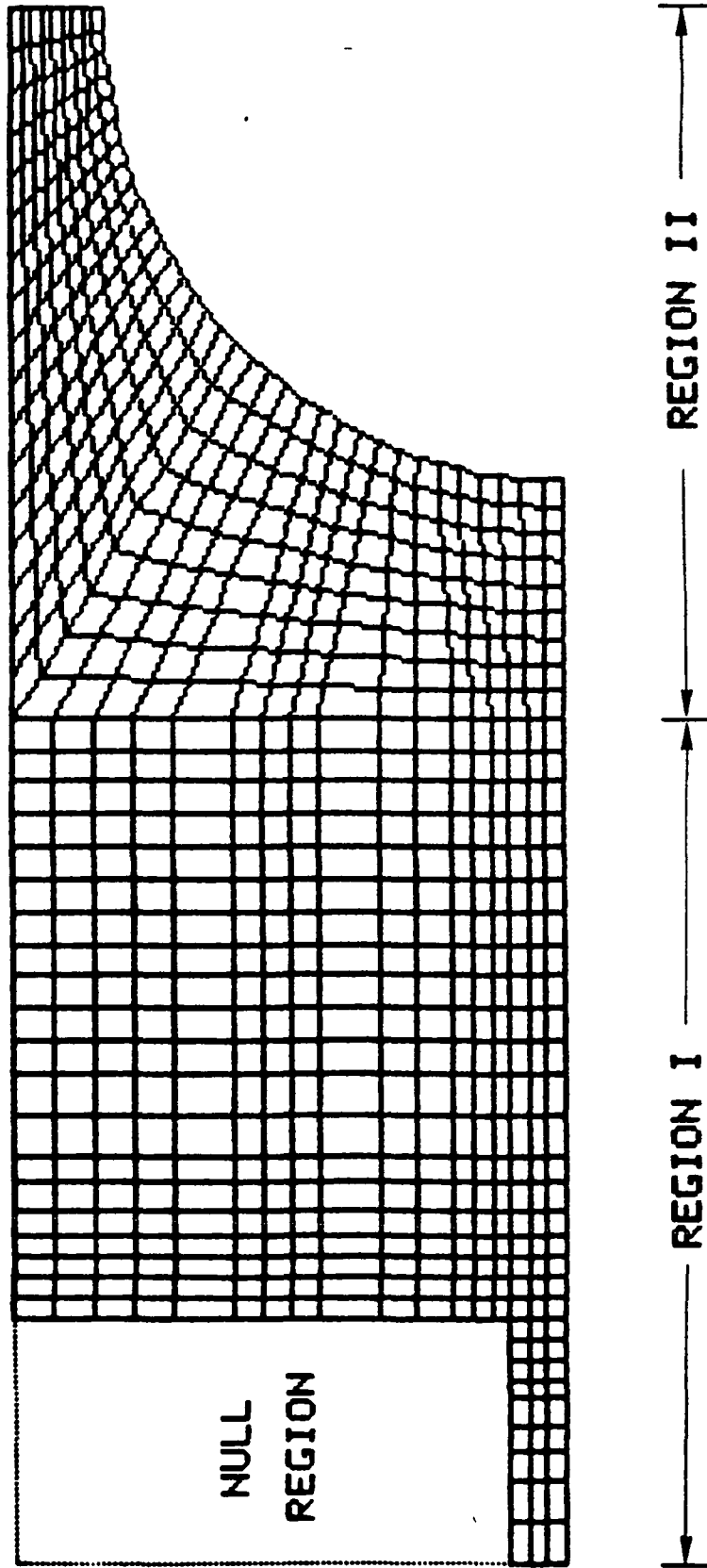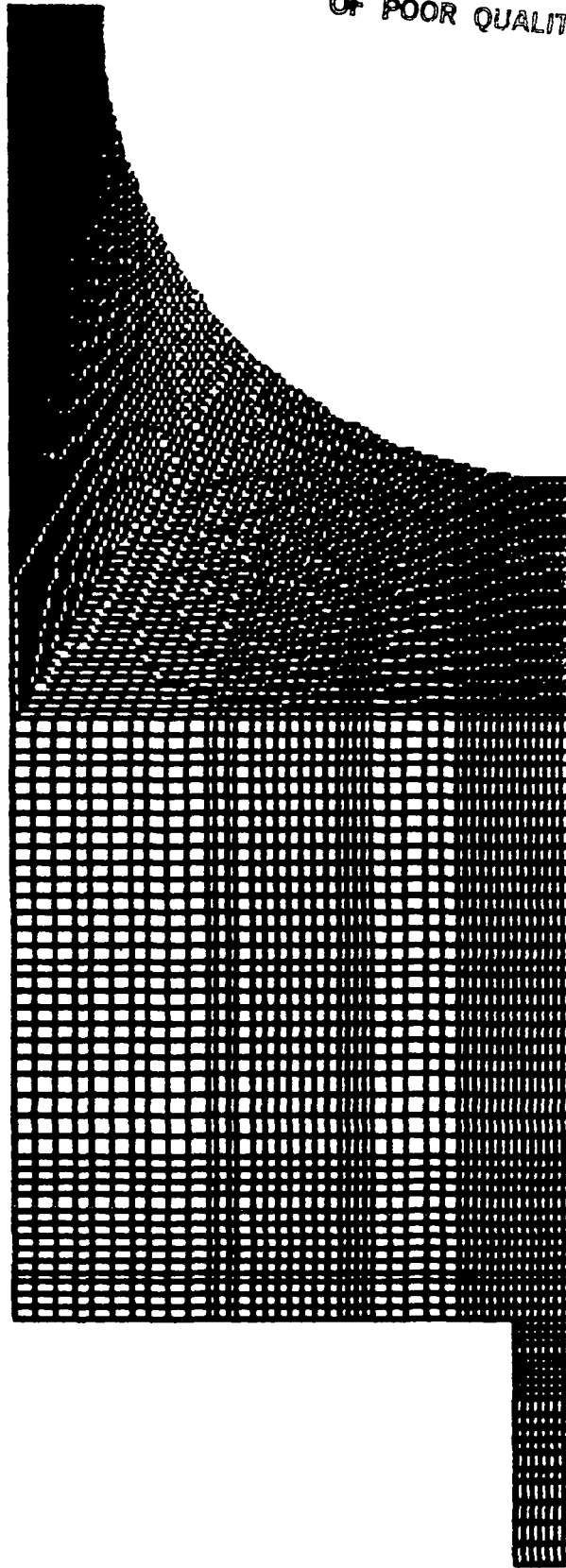
AXI-SYMMETRIC SSME FUEL PREBURNER COARSE GRID DEFINITION

Fig. 9 Axi-Symmetric SSME Fuel Preburner Coarse Grid (890 nodes) Definition

AXI-SYMMETRIC SSME FUEL PREBURNER FINE GRID DEFINITION

REGION III

REGION II

REGION I

Fig. 10 Axi-Symmetric SSME Fuel Preburner Fine Grid (5965 nodes) Definition

Boundary and Inlet Conditions

Adiabatic, free-slip conditions were assigned to all the combustion chamber walls on the assumption that the turbulent wall boundary layer is very thin and there is no heat transfer to the environment. Heat exchange across the preburner liner can be modeled, but this effect was not included in this study. One null region was used in the coarse grid definition. Table 3 shows the inlet and boundary conditions used for the axisymmetric model. Since the mixing near the injectors was described by the injector/lumping analysis a turbulent viscosity of 4.79 E-3 lb/ft-sec was obtained from equation 9 and was used throughout the combustion chamber. The same value of viscosity was also used in the three-dimensional analysis. The fuel/oxidizer equivalence ratios for the igniter flow zone, AB zone, CD zone and EFGH zone are 18, 9.5, 7.8 and 6.9 respectively. The injector simulation upstream boundary conditions were used for all four inlet zones. A fixed integrated mass flow boundary condition (FIMFBC) was used for the exit boundary.

Table 3 Inlet and Boundary Conditions for Axisymmetric Model

Zone	Igniter Flow	AB	CD	EFGH	Exit
$\dot{m}$ (lb/sec)	1.55	22.43	36.53	114.86	175.38
αH_2	0.65853	0.48678	0.43272	0.39854	-
αH_2O	0.34147	0.51322	0.56728	0.60141	-
T (°R)	1112.4	1796.4	2098.8	2298.6	-
P(lbf/ft^2)	798804	798804	798804	798804	-
P_0(lbf/ft^2)	1007452	947357	947357	947357	-
C_I	3.25E-4	6.45E-3	1.08E-2	3.45E-2	-
q (ft/sec)	191	257	282	333	-
B.C.	ISUBC	ISUBC	ISUBC	ISUBC	FIMRBC

Results for the Axisymmetric Fuel Preburner Models

Figure 11 shows the flow vectors for the coarse grid calculation. There is a flow stagnation region formed near the top of the fuel turbopump dome. The four streams of combusted products flowed down the combustion chamber and gradually merged with each other as the flow passage narrowed over the fuel turbopump dome. The flow speed of each streamline reached its maximum at the exit. The mass flow rate at each cross sectional plane of the fuel preburner was constant at steady state due to the fixed integrated mass flow rate boundary condition at the exit. The flow vectors of the fine grid calculation are similar to that of the coarse grid calculation.

The flow area contraction ratio of the main chamber to the exit is about three to one. The large flow area contraction ratio is reported to cause a high level of secondary recirculation (Ref. 14) and, therefore, has the tendency to smooth out temperature profile variations. Figure 12 and Fig. 13 show the computational results for the temperature profile and hydrogen mass fraction profile of the coarse grid calculation. The results seemed to support the expectation that the large flow area contraction ratio does indeed tend to cause the four streams of combustion flows to mix completely at the exit section of the fuel preburner.

The computational results of the fine grid calculation show the flow to be mainly streamline. The temperature profile in Fig. 14 showed that although a certain amount of mixing occurred, temperature variations did exist at the exit of the preburner. Streamlines of colder temperatures climbed over the fuel turbopump dome to the exit and so did the hot, outer combustion streamlines. An averaged, radial temperature profile at the exit (Fig. 15) showed a 300 °R variation. Figure 16 shows the result of the hydrogen mass fraction profile of the fine grid calculation. The mass fraction streamlines showed hydrogen mass fraction variations at the fuel preburner exit. The discrepancies between the results of the coarse grid calculation and those of the fine grid calculation show the effect of numerical diffusion due to discretization. The results of the fine grid calculation should be used as the input for turbine flowfield calculation. About 1000 CPU seconds were used for coarse grid case and 8000 CPU seconds were used for fine grid case on CYBER 205 to reach steady state.
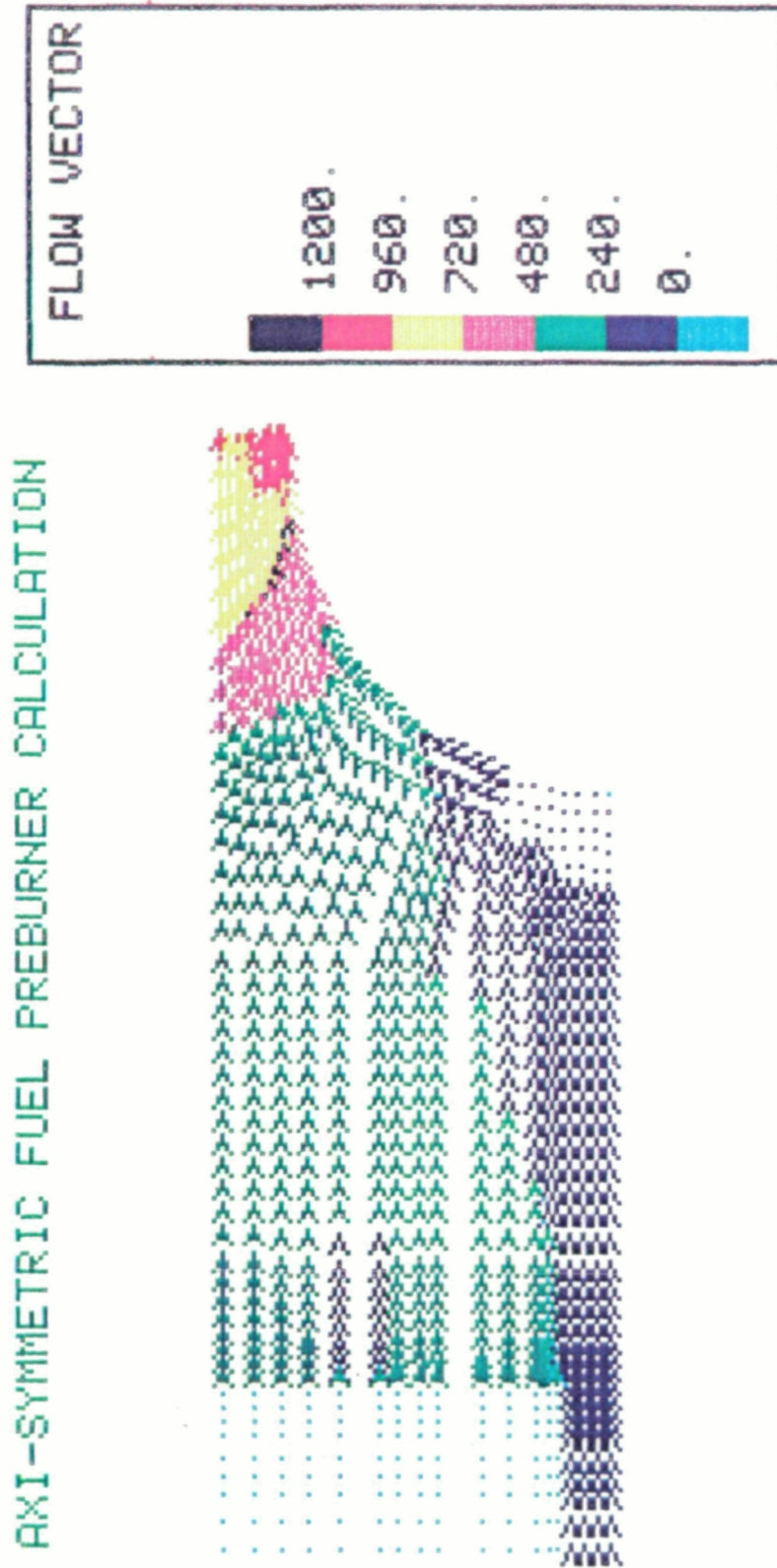
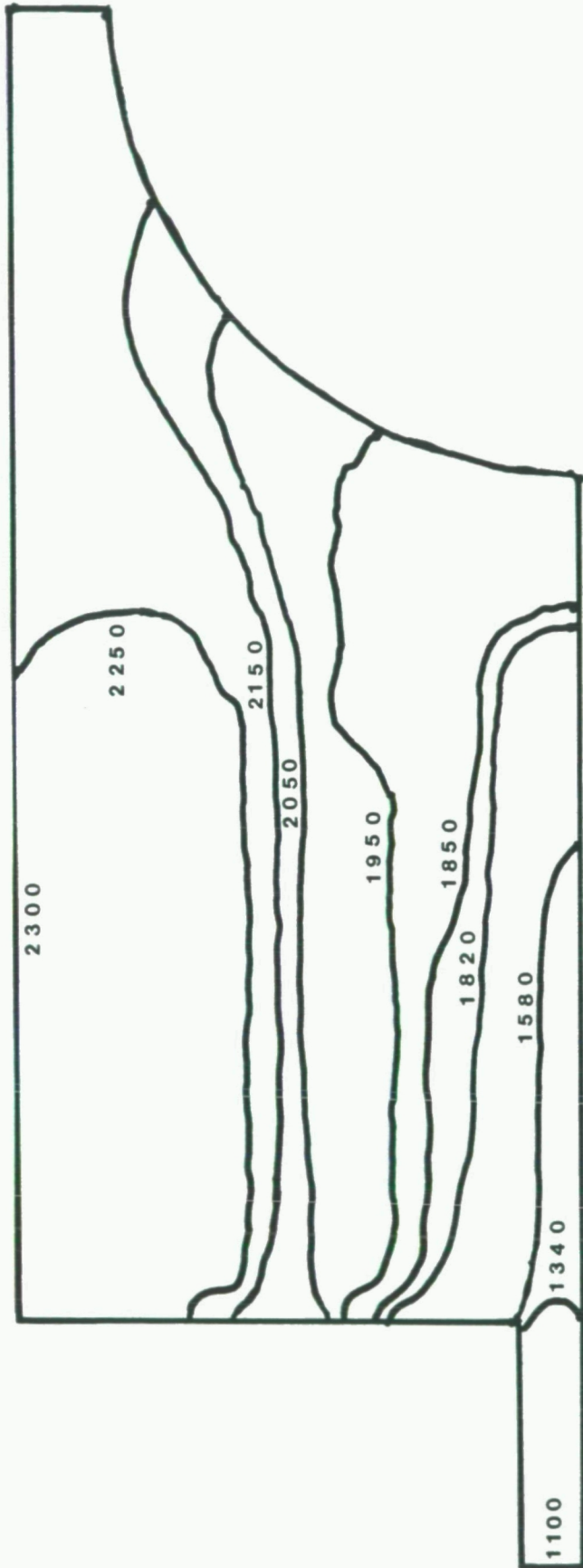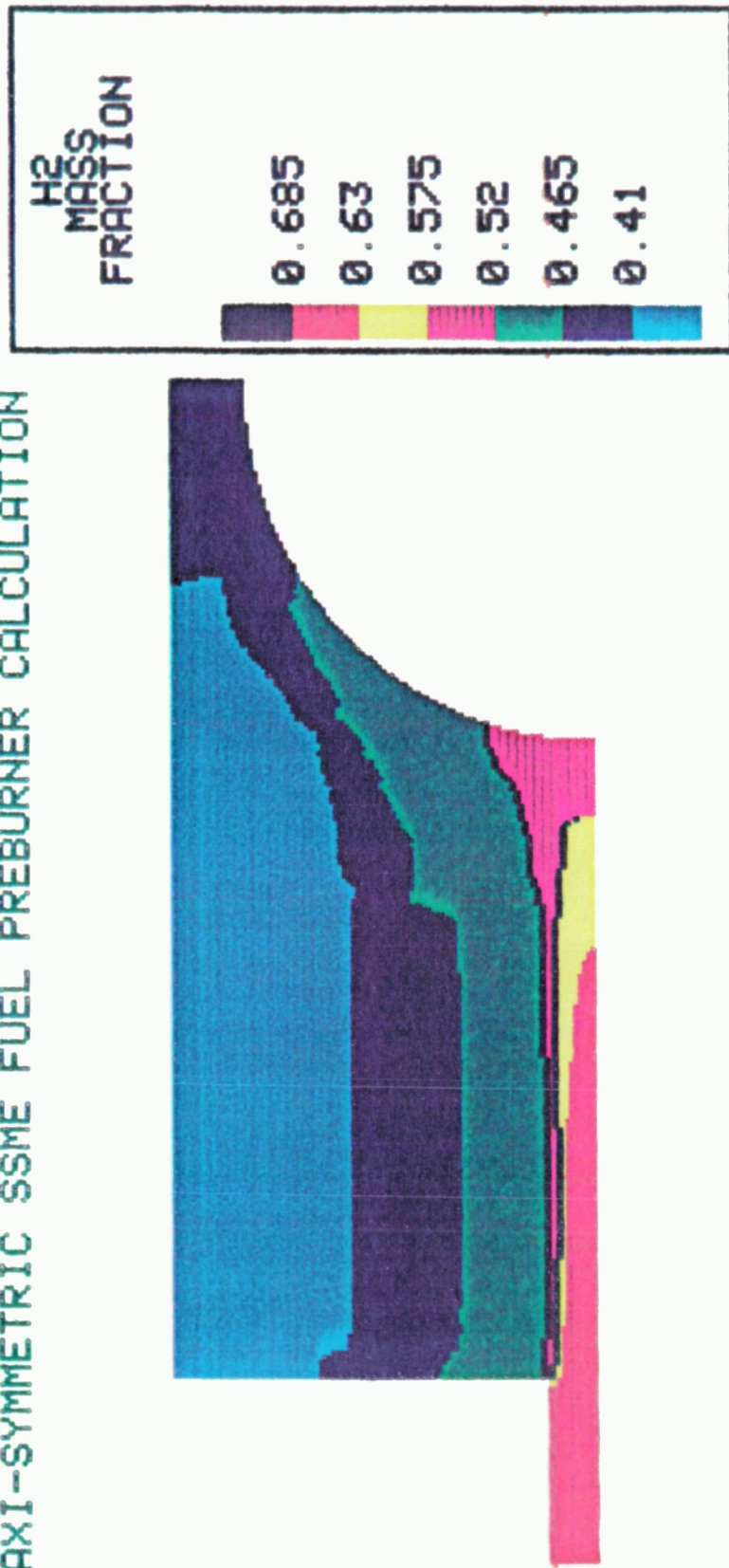Fig. 11 Axi-Symmetric SSME Fuel Preburner Flow Vector

Fig. 12 Axi-Symmetric SSME Fuel Preburner Temperature (Coarse Grid)

Fig. 13   Axi-Symmetric SSME Fuel Preburner Hydrogen Mass Fraction (Coarse Grid)
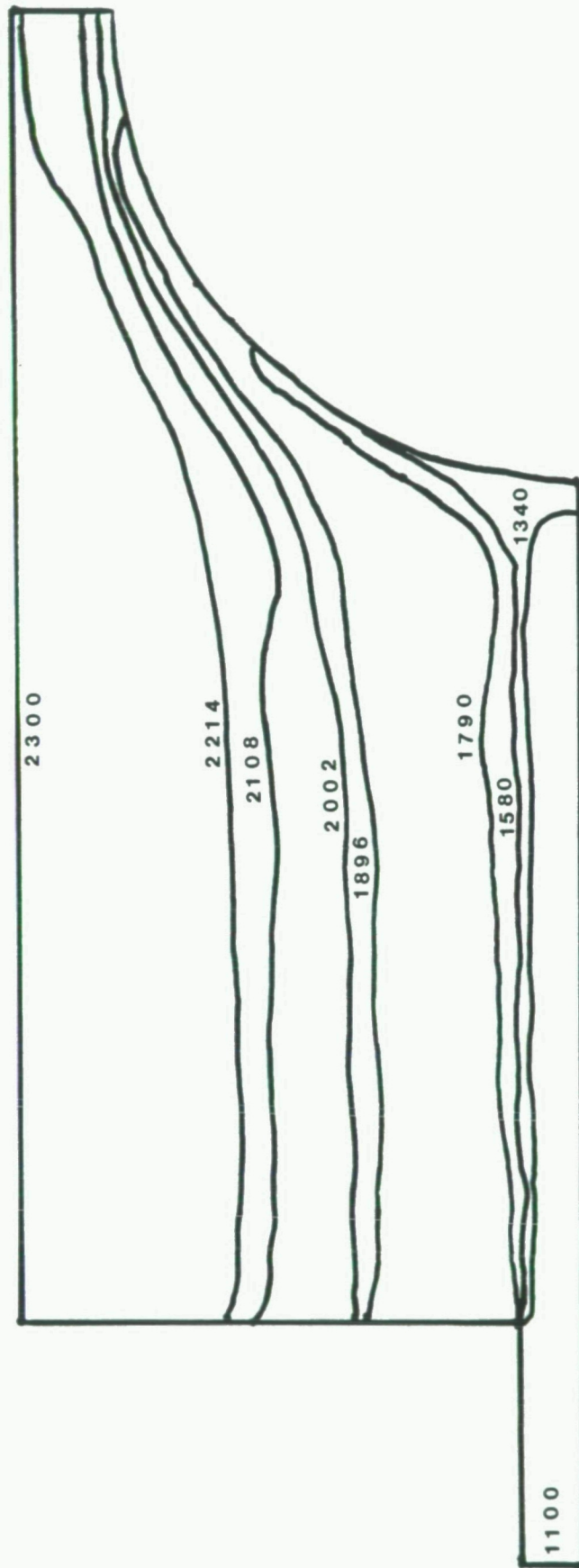
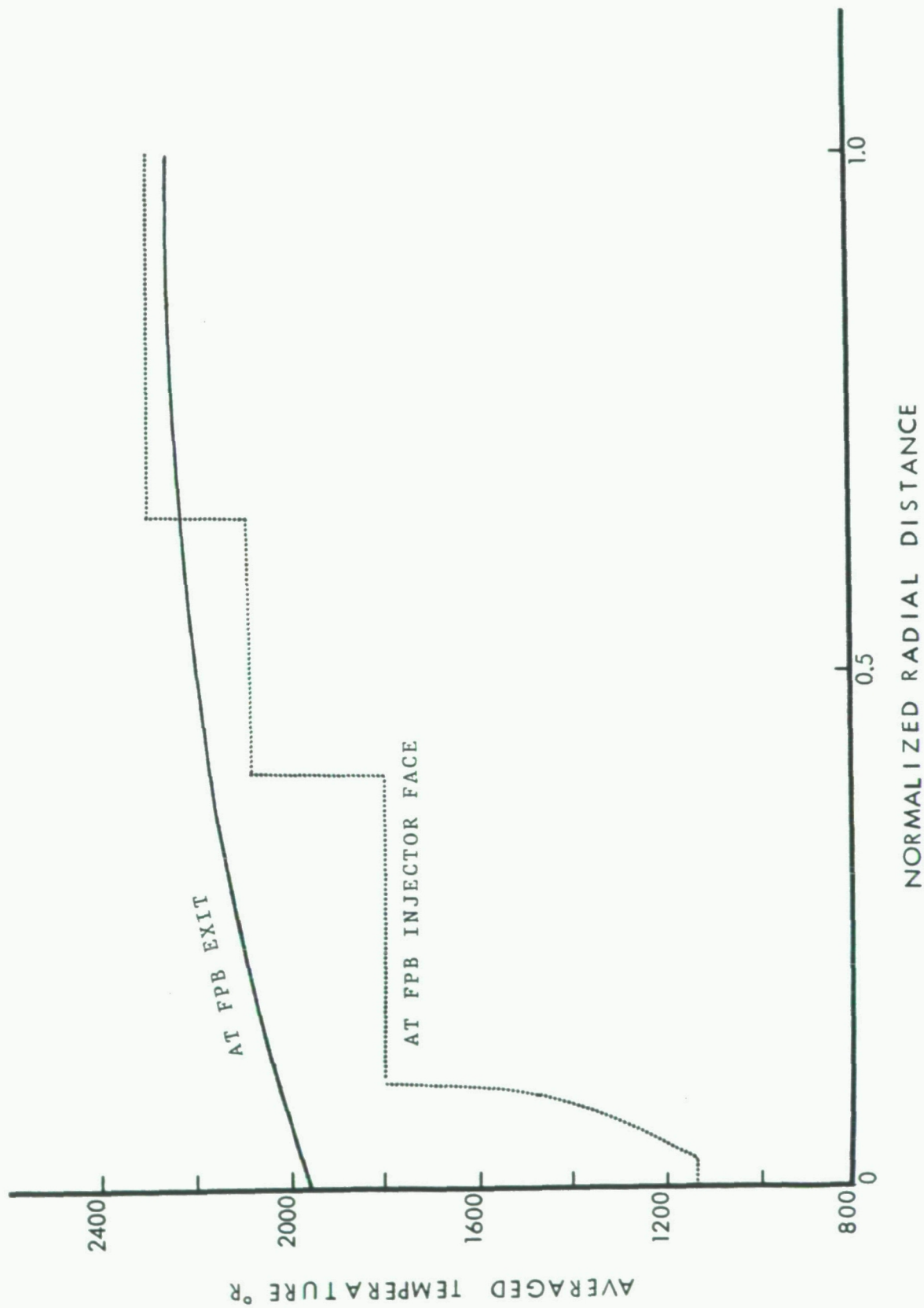Fig. 14 Axi-Symmetric SSME Fuel Preburner Temperature (Fine Grid)

2300

2214

2108

2002

1896

1790

1580

1340

1100

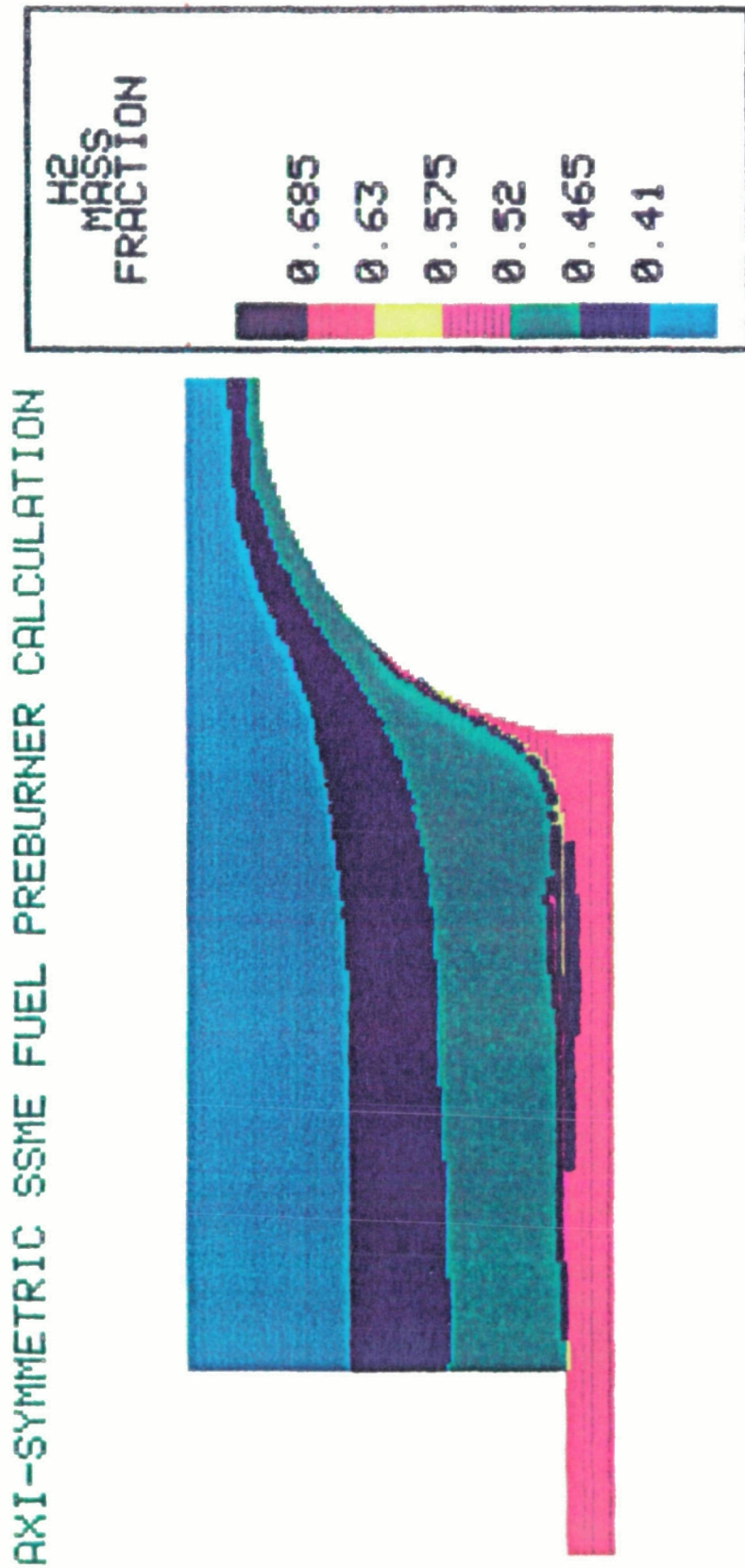Fig. 15 Axi-Symmetric SSME Fuel Preburner Inlet and Exit Temperature

Fig. 16   Axi-Symmetric SSME Fuel Preburner Hydrogen Mass Fraction (Fine Grid)

THREE-DIMENSIONAL MODELING OF THE FUEL PREBURNER

Grid Definition

Three grid regions were used to construct the grid system for three-dimensional fuel preburner modeling. A front view of the three-dimensional fuel preburner grid with a 30 deg. angle is shown in Fig. 17. Region I is the augmented spark igniter chamber; Region II comprises the major part of the fuel preburner combustion chamber, the injector faceplate and three flow-straightening cooling-baffles; Region III represents the flowfield for the combusted gases that flows around the hemispheric high pressure fuel turbopump dome and eventually leaves the fuel preburner exit to drive the turbines. The coordinate system is such that the η_3 coordinate coincides with the central axis of the fuel preburner, η_1 coordinate points radially from center to the wall, and η_2 coordinate goes circumferentially around the centerline. This way the 3-D grid system can be closed by starting with a slice of the 2-D grid system and move it axisymmetrically around the centerline for 360 deg. to overlap with the original 2-D slice. Region II and Region III have to be separated in order to get the exact sizes and shapes for the baffles and the hemispheric dome. Region I was separated from Region II to save a large number of nodes. Notice that there are no nodal points inside the turbopump dome. The total number of nodes used in the computation was 21,638.

Figure 18 shows a top view of the 3-D fuel preburner grid system. Baffle 1 is located at 330 deg. baffle 2 is located at 90 deg., and baffle 3 is located at 210 deg.
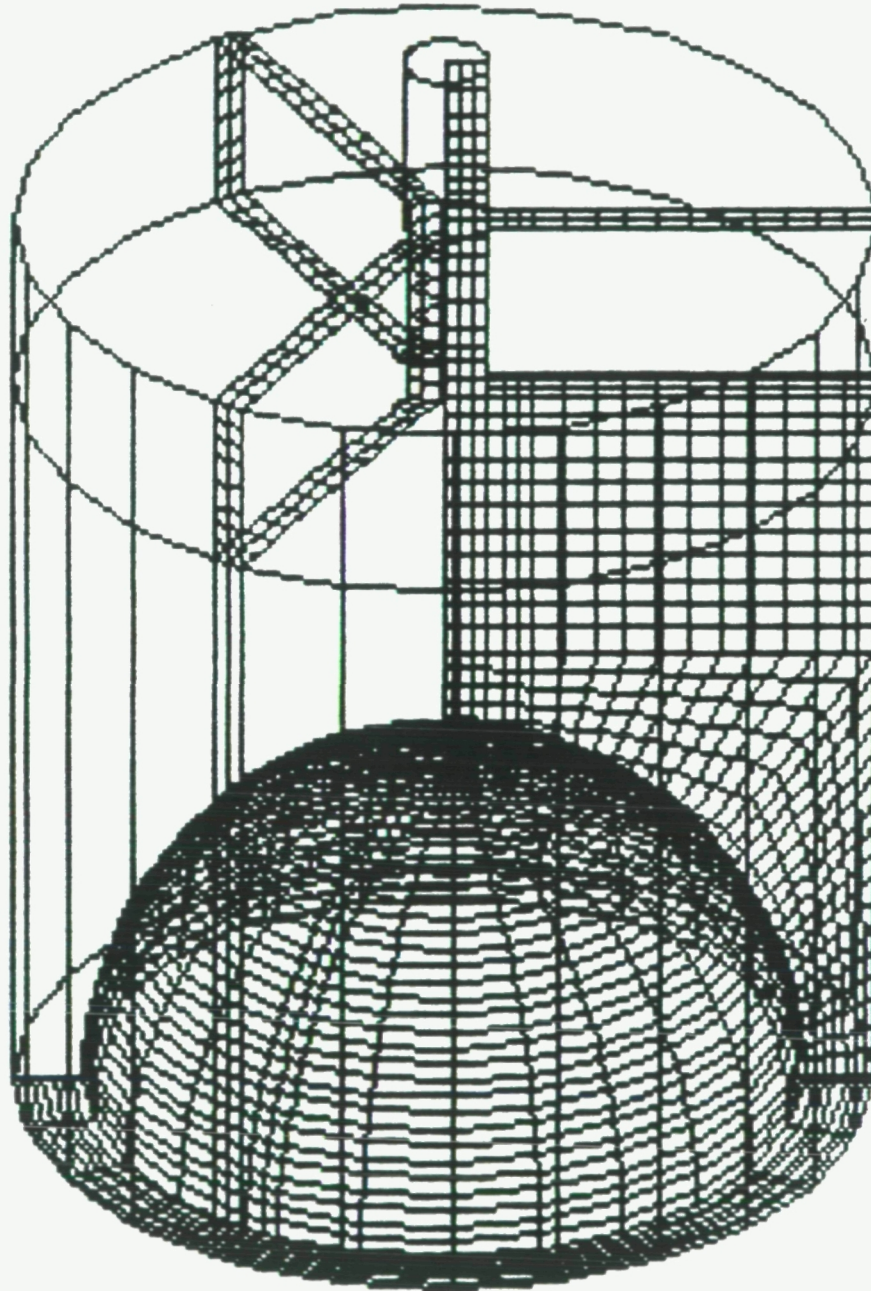
Fig. 17   Front View of the 3-D SSME Fuel Preburner
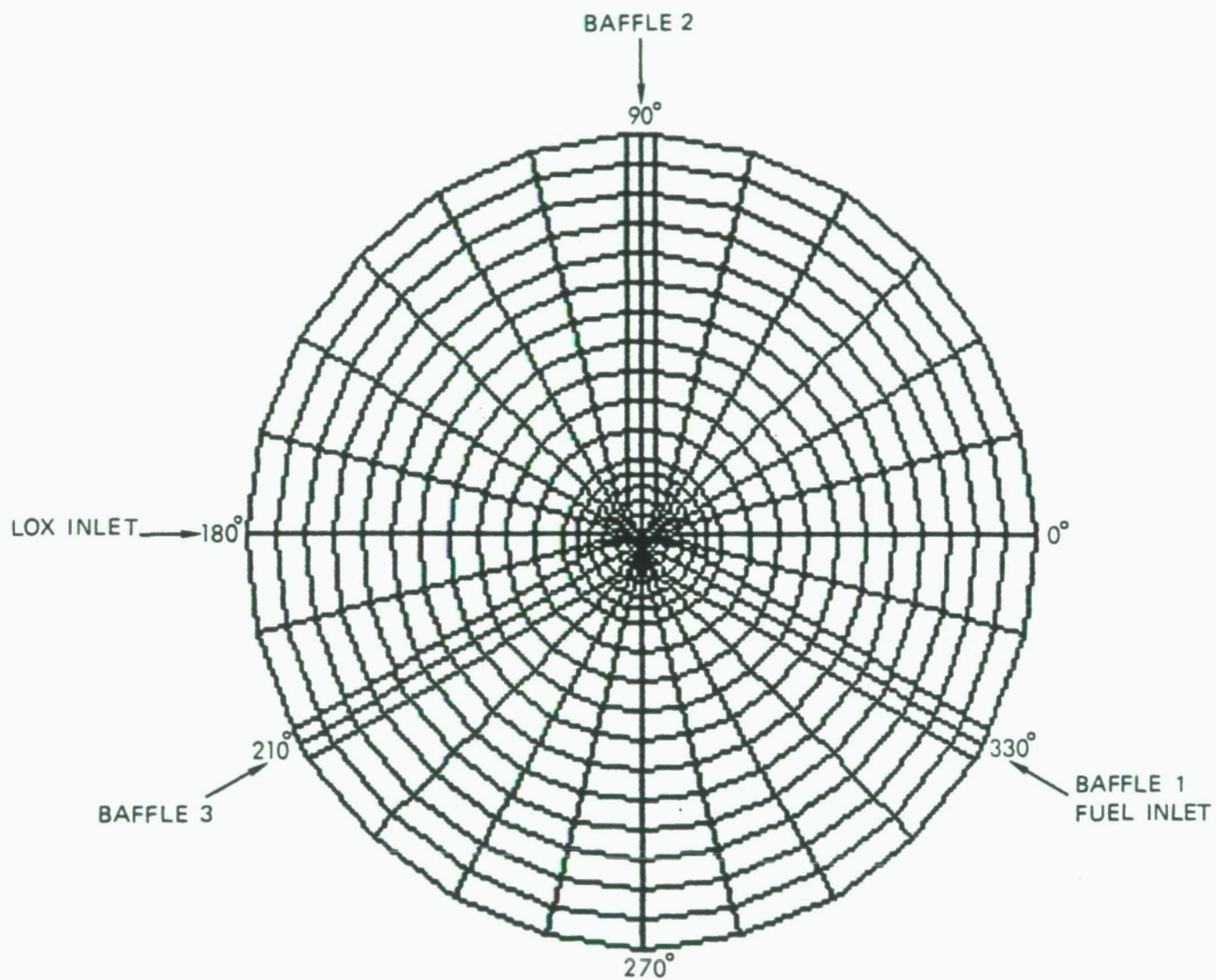   Grid Definition With a 30 Degree Angle

-40-

Fig. 18   Top View of the 3-D SSME Fuel Preburner Grid Definition

Boundary and Inlet Conditions

Adiabatic free slip conditions were assigned to all the combustion chamber walls for the purposes of this study. Null regions were assigned to the inside of the three baffles. Table 4 shows the inlet and boundary conditions for the three-dimensional model. The injector simulation upstream boundary condition was used on all four inlet combustion zones on the injector faceplate. A fixed inlet boundary condition was used for coolant hydrogen flow on the baffle. Fixed mass flow rate boundary conditions were applied to the exit. Swirling components were added to the ASI inlet velocity vectors to simulate hydrogen in flow.

Table 4 Inlet and Boundary Conditions for Three-Dimensional Model

Zone	Baffle Flow	Igniter Flow	AB	CD	EFGH	Exit
$\dot{m}$ (lb/sec)	3.15	1.55	20.98	35.97	113.73	175.38
$\alpha\, H_2$	1.0	0.65853	0.45129	0.42382	0.39259	–
$\alpha\, H_2O$	0.0	0.34147	0.54871	0.57618	0.60741	–
T (°R)	300	1112.4	1985.4	2143.8	2338.2	–
$P(lbf/ft^2)$	798804	798804	798804	798804	798804	–
$P_0(lbf/ft^2)$	–	1007452	947357	947357	947357	–
C_I	–	3.25E-4	6.16E-3	1.07E-2	3.43E-2	–
$q(ft/sec)$	59	191	398	284	417	–
B.C.	FIBC	ISUBC	ISUBC	ISUBC	ISUBC	FIMRBC

Results for the Three-Dimensional Fuel Preburner Model

The three-dimensional model provides more insight into the fuel preburner operation than the axisymmetric model in that swirling ASI flow effects, baffle flow straightening effects, baffle coolant flow effects and asymmetric flow effects due to unbalanced heating or cooling can be studied. Figure 19 shows the swirling components of the ASI inlet flow. The swirling comes from the eight tangential fuel injectors around the center oxidizer jets. The rich swirling ASI flow not only ignites the main injector flow but also protects the ASI combustion chamber walls. Figure 20 shows a three-dimensional plot view of the flow vectors. Seven slices of the grid system constitute the plot view with a 30 deg. front view angle. The plot view consists of a section of the ASI inlet, a section of the injector faceplate, the left section of the outside wall, an internal section which contains the baffle, another internal piece which sits between two baffles, a section of the surface of the turbopump and the exit. The rectangular area in one of the internal sections is one of the baffles. There is a stagnated flow region near the top of the turbopump dome. The coolant hydrogen flow comes down the baffle slowly and mixes gradually with bulk flow while accelerating toward the exit. The slice of the internal flow located between two baffles looks similar to that of an axisymmetric calculation. The swirling component of ASI flow loses its momentum below the injector faceplate, partially due to the baffle flow straightening effect, and partially due to its small flow rate.

Figure 21 shows the temperature contours for the same plot view. The cooling effect of the baffle coolant flow can be seen clearly from the internal section on the right. The 1850 °R isotherm traced on the surface of the turbopump dome shows a combined influence from the igniter flow and the coolant baffle flow. The lack of variation in temperature gradient at the exit indicates the existence of a coarse grid smearing effect. Figure 22 shows a cross-sectional view of temperature contours at the bottom of the baffles. The residual effect of the swirling can be seen close to the baffles. Figure 23 shows another cross-sectional view 1.63 in. above the top of the turbopump. The cooler temperature indicates the influence of the baffle coolant flow.

Figure 24 compares the predicted circumferential temperature profile near the preburner exit with that from hot fire test data (Ref. 14). The hot fire test was conducted with SSME component preburner assemblies. The preburner was assembled with a nozzle assembly which acted as a turbine simulator. The thermocouple ports in the test were

located on two planes in the turbine inlet zone. Twenty-four temperature sensing positions were located in the lower plane which was approximately 10.75 in. downstream from the injector face. Half of them were installed with sensing tips extending into the discharge nozzles, and the temperatures obtained are called "nozzle" temperatures. The remaining half were located midway between discharge nozzle and are called "standard" temperatures. Sixteen additional thermocouple ports were equally spaced around the nozzle assembly on a plane about 9.5 in. from the injector face. These are referred to as "special" temperatures. The predicted temperature profile is an average of the temperatures of the nodes in between these two planes. The predicted temperature profile showed similar trends to those of test data. The temperatures are near their minimum under the baffles, and are near their maximum in between baffles. The predicted temperatures are somewhat higher than those of the test data. This is because the hot fire test was operated at an earlier version of the design which has a higher fuel/oxidizer equivalence ratio of 8.96 rather than the 7.65 used by the present computation. Nevertheless, the agreement of the trend and the closeness of the data level verify the validity of the model. This run takes about 29,000 CPU seconds on the CYBER 205 to reach steady state.

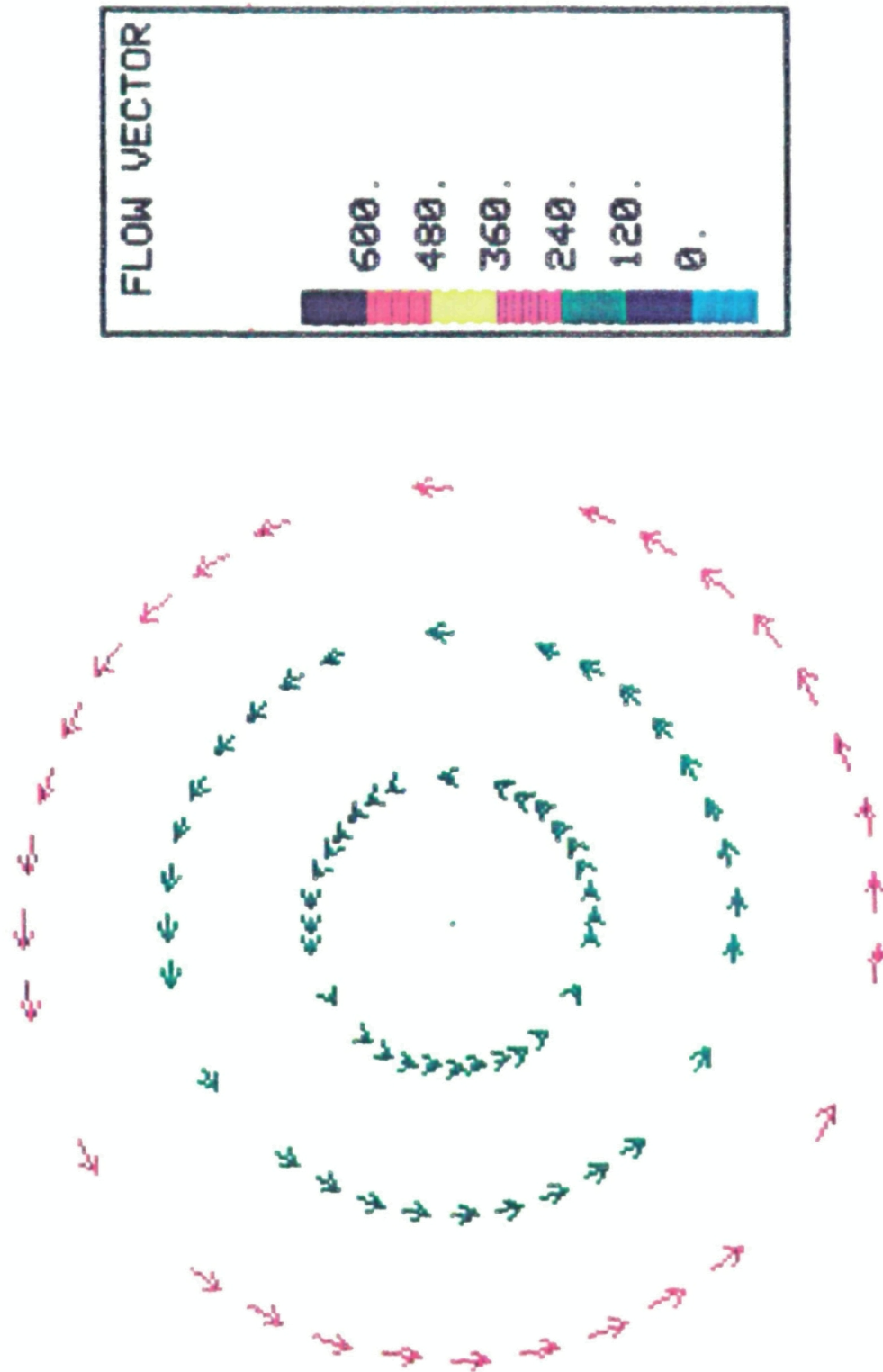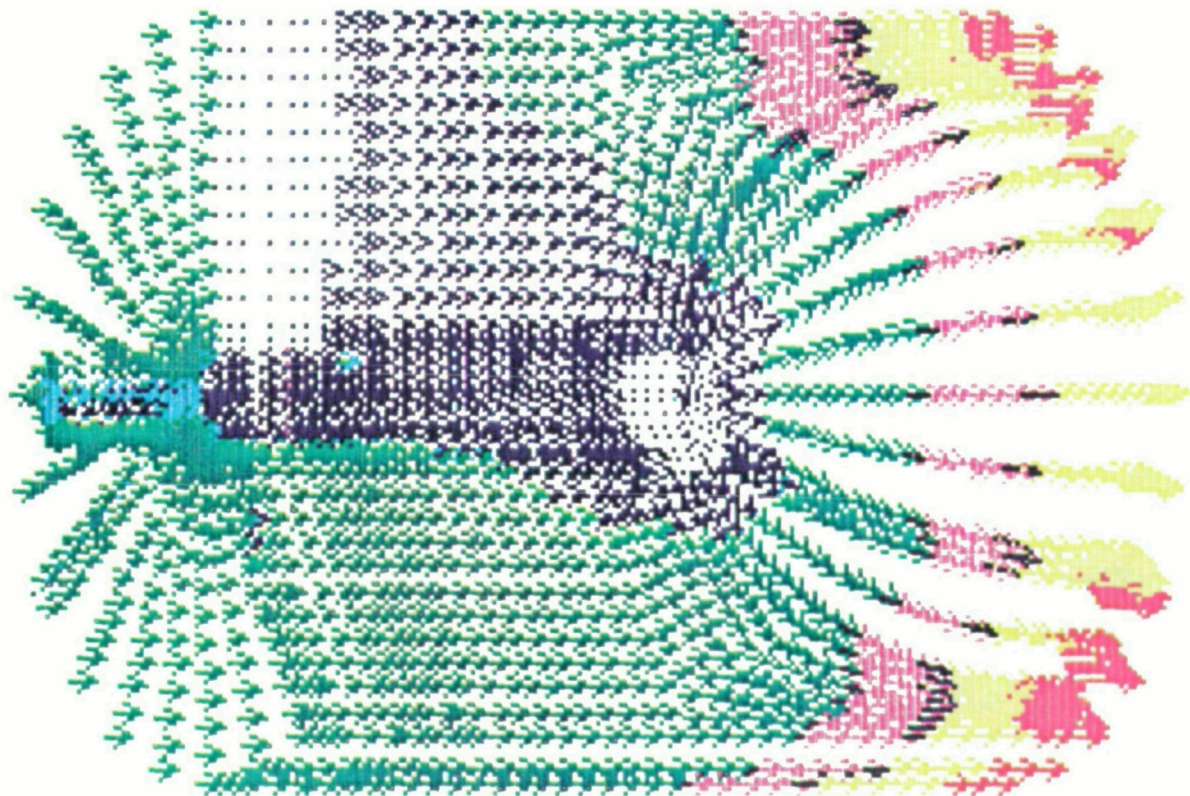SSME FUEL PREBURNER IGNITER INLET SWIRLING COMPONENTS

Fig. 19   The Swirling Flow Vector Component of the Igniter Inlet

FLOW VECTOR

1100.
880.
660.
440.
220.
0.

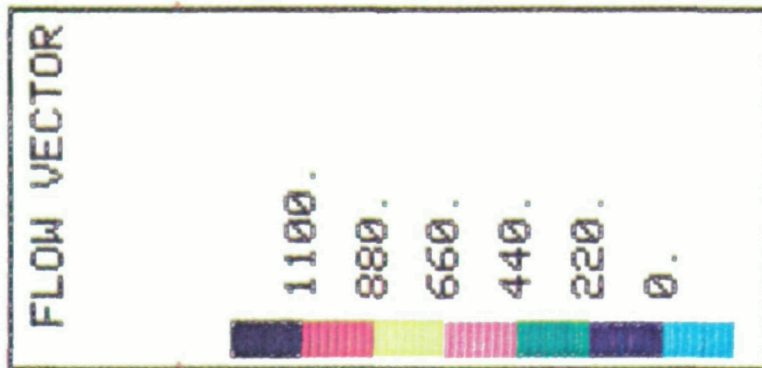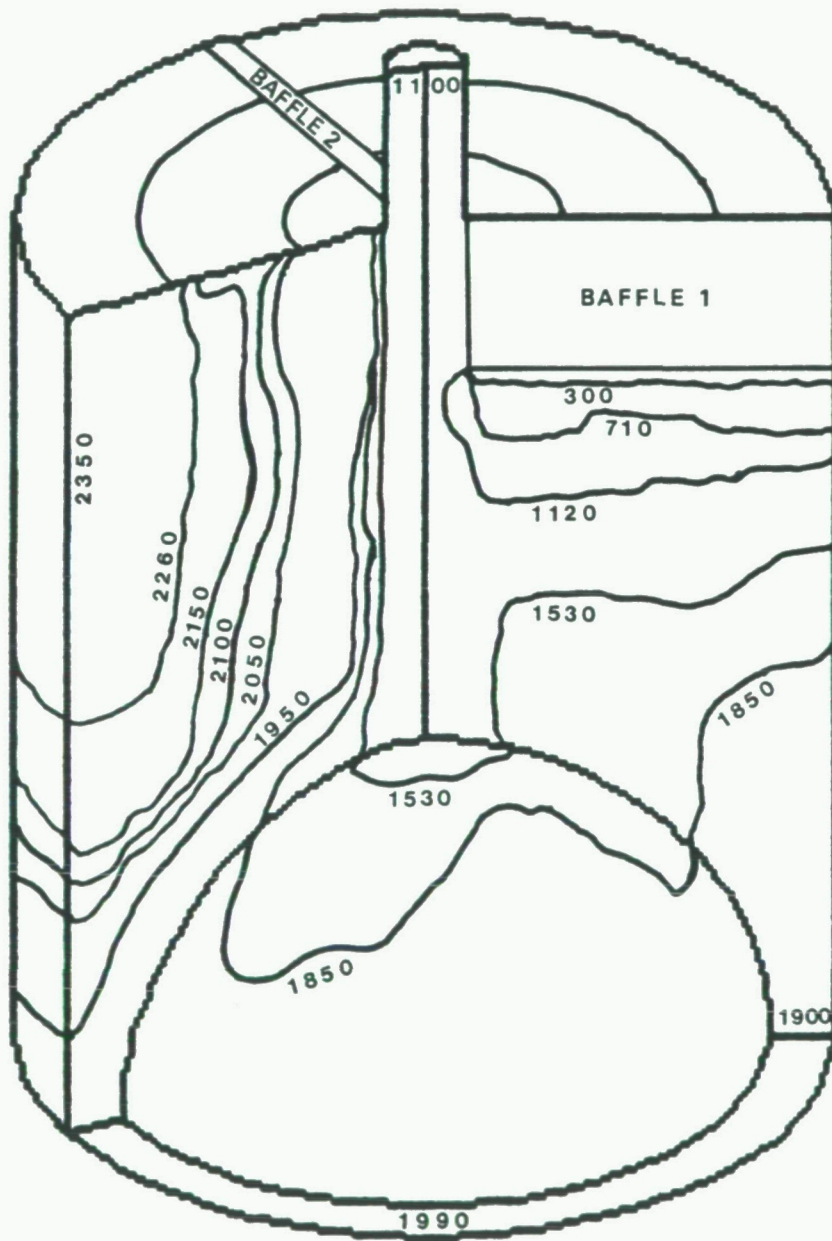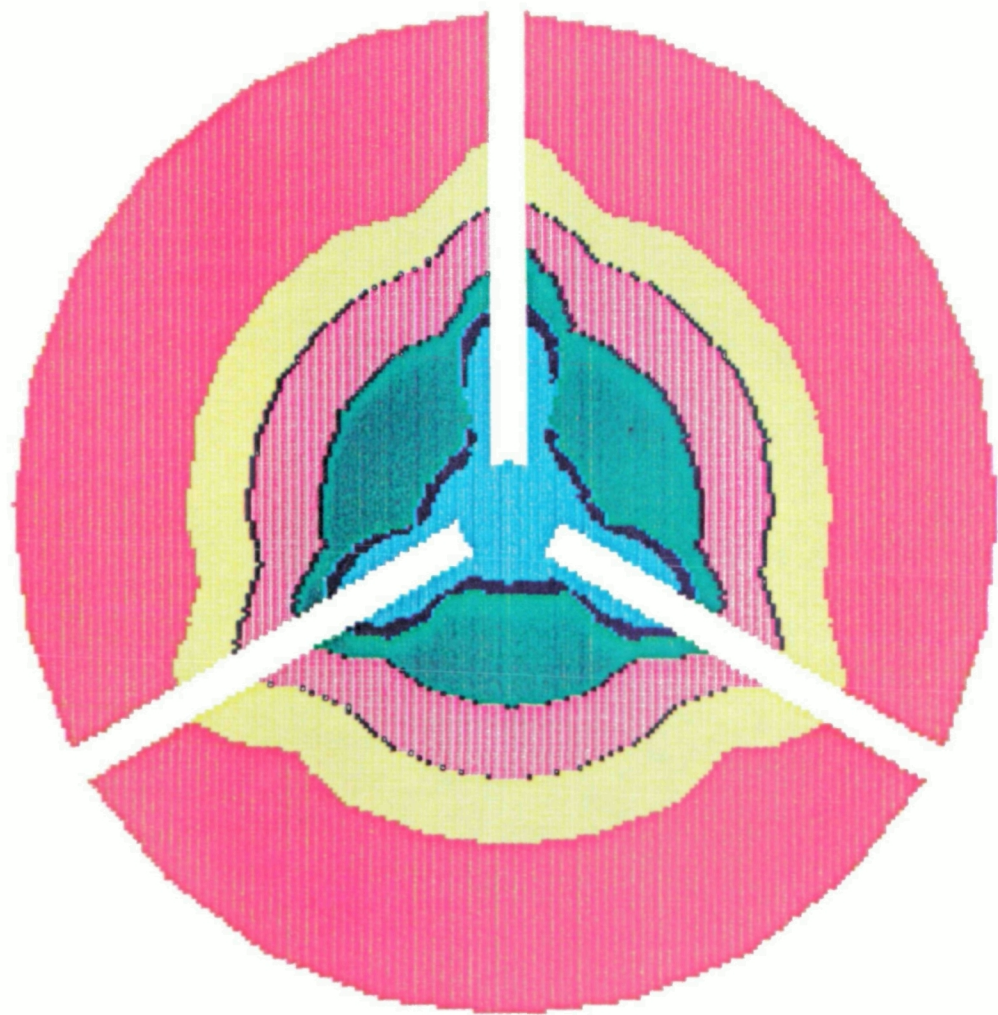3D FUEL PREBURNER CALCULATION

Fig. 20 3-D SSME Fuel Preburner
Flow Vector

Fig. 21   3-D SSME Fuel Preburner Temperature

3D SSME FUEL PREBURNER TEMPERATURE
CROSS-SECTIONAL VIEW AT BOTTOM OF BAFFLES

TEMPERATURE

2350.
2260.
2170.
2080.
1990.
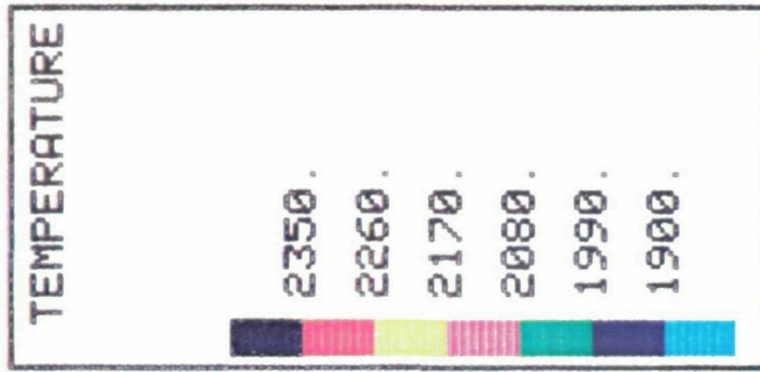1900.

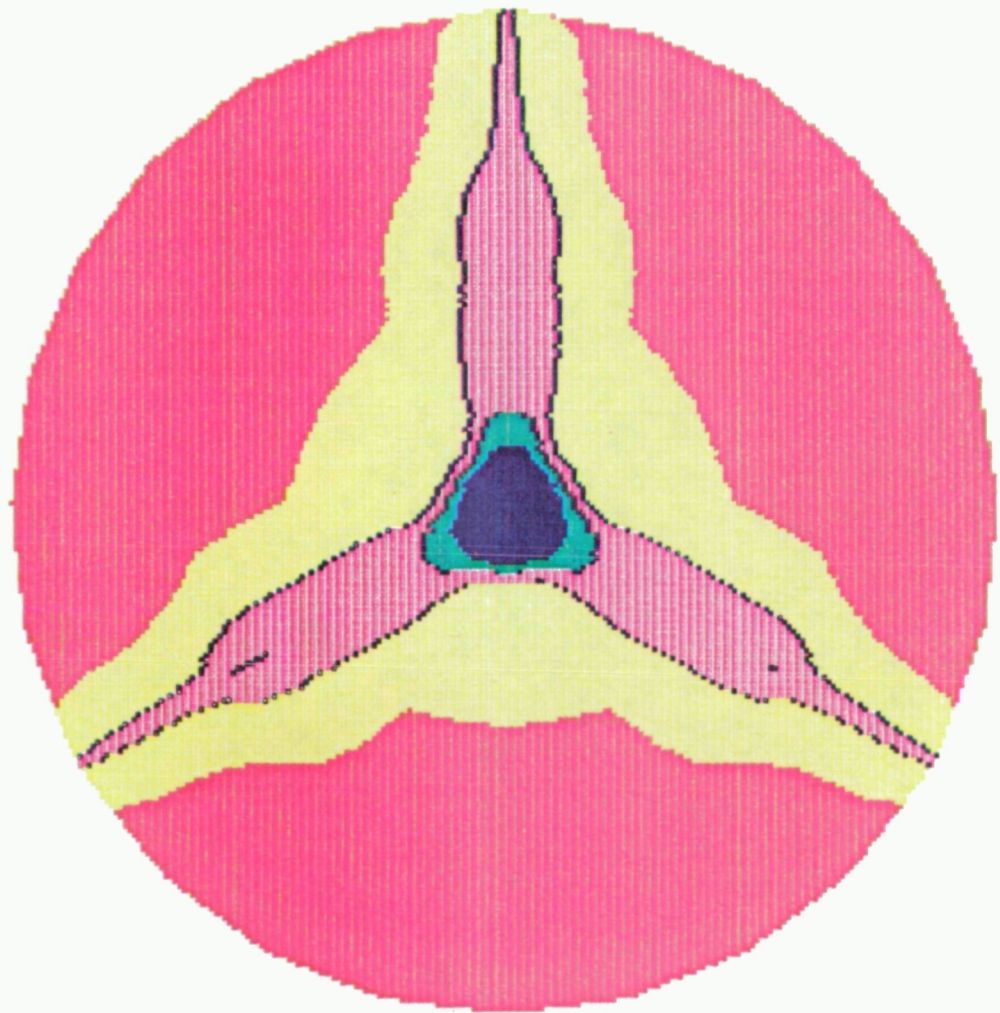ORIGINAL PAGE
COLOR PHOTOGRAPH

Fig. 22   3-D SSME Fuel Preburner Cross-Sectional Temperature at Bottom of Baffles

-49-

30 SSME FUEL PREBURNER TEMPERATURE

A CROSS-SECTIONAL VIEW ABOVE TURBO-PUMP

TEMPERATURE

2300.
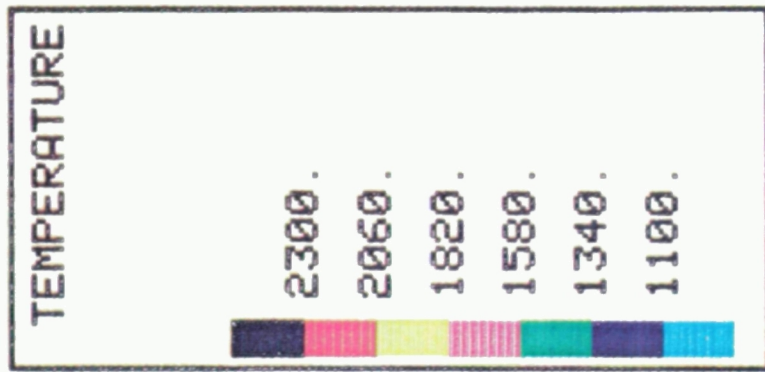2060.
1820.
1580.
1340.
1100.

Fig. 23   3-D SSME Fuel Preburner Cross-Sectional Temperature at 1.63 Inches Above Turbopump
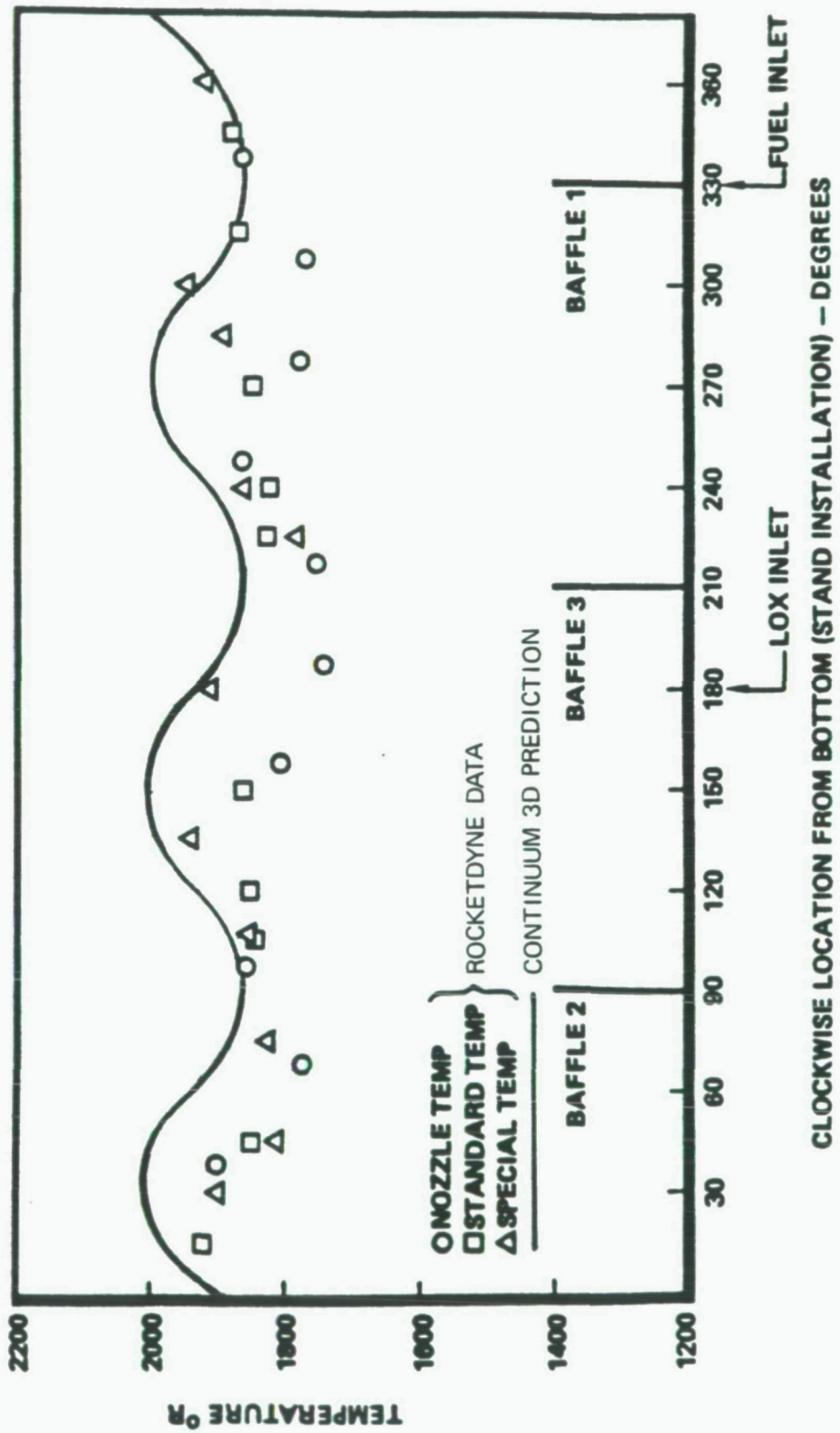
Fig. 24 SSME Fuel Turbine Inlet Temperature Profile at FPL

CONCLUSIONS

1. The result of a recent paper (Ref. 2), concerning the analysis of a single SSME fuel preburner injector element, has confirmed our model assumptions about fast atomization, immediate vaporization and instantaneous combustion in the fuel preburner. They found a short liquid jet length of about 2 cm, and the existence of few droplets beyond the tip of the liquid jet. The length of 2 cm amounts to just 6 percent of the total length of the fuel preburner chamber. The fact that the curves for percentage oxidizer atomization, vaporization and reaction reached 100 percent at 2 cm below the injection inlet and are practically identical, points out the instantaneous nature of vaporization and combustion during preburner operation.

2. The agreement in trend and data level of the circumferential exit temperature between the three-dimensional model and hot fire test data supports the accuracy of the computational model.

3. Due to the high rate of atomization, immediate vaporization and instantaneous combustion, no oxygen can survive the length of the combustion chamber to reach the Kaiser Hat on the top of the turbopump dome, or move into the convergent section and escape to burn turbine blades. The steady state flowfield of the preburner should be as our model suggests: striated combustion flows come down from the injector faceplate with hotter temperatures toward the outside wall due to the layout of the injectors, is cooled by coolant hydrogen from three equally spaced baffles, converges as it enters the convergent section and finally leaves for the turbines. The rich igniter flow produces colder flow, which not only protects the igniter chamber wall, but also cools down the turbopump dome surface. Therefore, there are no apparent hot spots formed during the steady state operation, although the axisymmetric model predicted temperature variation on the exit. The model assumes instantaneous mixing of the near injector region, and the turbulent calculation indicates very little additional mixing as the flow moves downstream. This important observation should be experimentally verified.

4. Local hot spots on the turbine blades are postulated to come from transient operation, i.e. flow leads and lags may cause near stoichiometric mixtures downstream of the preburner during start-up of the engine.

5. The SSME fuel preburner flowfield was successfully modeled by axisymmetric and three-dimensional models. The model generates realistic flows that can be used to understand the complicated preburner flowfield and aid the assessment of the design modifications.

RECOMMENDED MEASUREMENTS STUDY

As a result of flowfields described by the analyses reported herein, the following measurements are recommended:

1. The large temperature and mixture ratio gradients which are predicted at steady-state should be verified by direct measurements. Since it is very difficult to insert adequate probes for such measurements, optical emission/absorption measurements using fiber optics as radiation paths should be considered. The Test Bed Engine program may be used to accomplish these measurements.

2. Transient preburner exit temperatures should be measured in the test bed engine program.

3. The large differences seen in near-injector mixing and in highly turbulent parallel stream mixing should be investigated experimentally in a geometrically simple combustor. A laboratory combustor flow in which a few, easily varied injector elements can be used should be studied. Transparent side walls should also be used. The turbulent mixing and reaction progress must be quantitatively measured both optically and with probes.

REFERENCES

1. Space Transportation System Technical Manual - SSME Description and Operation, E41000/RSS-8559-1-1-1, Rocketdyne Division, Rockwell International Corporation, 5 April, 1982.

2. Liang, P.Y., R.J. Jensen and Y.M. Chang, "Numerical Analysis of SSME Fuel Preburner Injector Atomization and Combustion Processes," paper presented at AIAA conference, Reno, Nevada, January 1986.

3. (a) Prozan, R.J., "A Variational Principle for Compressible Fluid Mechanics: Discussion of One-Dimensional Theory," NASA CR3526 1982.

    (b) Prozan, R.J., "A Variational Principle for Compressible Fluid Mechanics: Discussion of the Multi-Dimensional Theory", NASA CR3614, 1982.

4. Prozan, R.J., "Hypothesis of a Variational Principle for Compressible FLuid Mechanics", CI-TR-0086, 1985.

5. Sindir, M.M., and P.T. Harsha, "Assessment of Turbulence Models for Scramjet Flowfields", NASA CR3643, 1982.

6. Eggers, J.M., "Turbulent Mixing of Coaxial Compressible Hydrogen-Air Jets", NASA TN D-6487, 1971.

7. Abramovich, G.N., The Theory of Turbulent Jets, MIT Press, 1963.

8. Wang, T.S. and R.C. Farmer, "Computational Analysis of the SSME Fuel Preburner Flow," Interim report, CI-IR-0078, January 21, 1985.

9. Chriss, D. and R.A. Paulk, "An Experimental Investigation of Subsonic Coaxial Free Turbulent Mixing", AFOSR-TR-72-0237, 1972.

10. Edelman, R.B., R.C. Farmer, and T.S. Wang, "Combustion and Emissions of Synthetic Fuel Components, Analysis and Modeling", Combustion of Synthetic Fuels (W. Bartok, ed.) ACS Symposium Series 217, American Chemical Society, pp. 29-48, 1983.

11. Rogers, R.C. and W. Chinitz, "Using a Global Hydrogen-Air Combustion Model in Turbulent Reacting Flow Calculations", AIAA Journal, Vol. 21, No. 4, pp.586-592, 1983.

12. Smith, J.M. and H.C. Van Ness, Introduction to Chemical Engineering Thermodynamics, 3rd edition, McGraw Hill, Inc., 1975.

13. Rabin, E. and R.B. Lawhead, "The Motion and Shattering of Burning and Non-Burning Propellant Drops," AFOSR-TN-59-129, 1959.

14. Fleck, D.L., "Design Verification Complete Package—Hot Gas Temperature," RSS-305-22, October 23, 1979.